



HAL
open science

Paleoproterozoic collision tectonics in West Africa: Insights into the geodynamics of continental growth

Kalidou Traoré, Dominique Chardon, Séta Naba, Ousmane Wane, Mamadou
Lamine Bouaré

► **To cite this version:**

Kalidou Traoré, Dominique Chardon, Séta Naba, Ousmane Wane, Mamadou Lamine Bouaré. Paleoproterozoic collision tectonics in West Africa: Insights into the geodynamics of continental growth. *Precambrian Research*, 2022, 376, pp.106692. 10.1016/j.precamres.2022.106692 . hal-04525946

HAL Id: hal-04525946

<https://hal.science/hal-04525946>

Submitted on 29 Mar 2024

HAL is a multi-disciplinary open access archive for the deposit and dissemination of scientific research documents, whether they are published or not. The documents may come from teaching and research institutions in France or abroad, or from public or private research centers.

L'archive ouverte pluridisciplinaire **HAL**, est destinée au dépôt et à la diffusion de documents scientifiques de niveau recherche, publiés ou non, émanant des établissements d'enseignement et de recherche français ou étrangers, des laboratoires publics ou privés.

1 **Paleoproterozoic collision tectonics in West Africa:**
2 **Insights into the geodynamics of continental growth**

3
4
5 **Kalidou Traoré^{1,2}, Dominique Chardon^{1,3*}, Séta Naba¹, Ousmane Wane⁴,**
6 **Mamadou Lamine Bouaré⁵**

7
8 ¹ Laboratoire Géosciences et Environnement (LaGE), Université Joseph Ki-Zerbo, Ouagadougou, Burkina
9 Faso

10 ² Laboratoire de cartographie, D.E.R de Géologie, FST,
11 Université des Sciences, des Techniques et des Technologies de Bamako, Bamako, Mali

12 ³ GET, Université de Toulouse, IRD, CNRS, UPS, CNES, France

13 ⁴ Laboratoire de Minéralogie et de Pétrologie, D.E.R de Géologie, FST,
14 Université des Sciences, des Techniques et des Technologies de Bamako, Bamako, Mali

15 ⁵ Ecole Nationale d'Ingénieur Ahmed Baba Touré, Bamako, Mali
16
17

18 **Cite this paper as:**

19 **Traoré, K., Chardon, D., Naba, S., Wane, O. Bouaré, M.L., 2022. Paleoproterozoic**
20 **collision tectonics in West Africa: Insights into the geodynamics of continental**
21 **growth. *Precambrian Research* 376, 106692.**
22 **<https://doi.org/10.1016/j.precamres.2022.106692>**

23
24
25 * Corresponding author: Dominique Chardon (dominique.chardon@ird.fr)
26

27 **Highlights:**

- 28 - Transpressional collision of the Eburnean accretionary orogen and its flanking craton
- 29 - Collision absorbed through a multi-scale anastomosed shear zone network
- 30 - Oblique shearing of the cratonic margin and indentation of the accretionary orogen
- 31 - Lithospheric delamination at craton edge enabling HP-HT collisional orogeny
- 32 - Enhanced syn-collisional juvenile magmatic accretion at the expense of the craton

33

34 **Abstract**

35 In order to decipher the collision processes between the Eburnean (Paleoproterozoic)
36 accretionary orogen and its flanking Archean craton, photointerpretation was combined
37 with the extraction of structural data from geological quadrangle maps to draw the
38 structural pattern of the southern West African craton. This pattern reveals multi-scale
39 transpressive anastomosing shear zone networks affecting both the Eburnean orogen
40 and its Archean buttress that absorbed protracted E-W convergence as juvenile crust
41 was still being accreted. Collision involved oblique transcurrent shearing of the craton
42 margin that led to the asymmetrical indentation and escape of the accretionary orogen.
43 As part of the collisional deformation pattern, the craton margin developed a narrow
44 orogenic system recording intense transpressional strain and high pressure-high
45 temperature metamorphism. Lithospheric mantle delamination at the craton margin
46 explains focused heat advection and extreme thermal softening of the crust, enabling
47 steep narrow transpressional collisional orogeny at the rear of accretionary orogens.
48 Delamination also provides a mechanism for the growth of accretionary orogens at the
49 expense of their flanking cratons.

50

51 **Keywords:** Hot orogen; Accretionary orogen; Transpression; Eburnean;
52 Transamazonian; Delamination

53

54 **1 Introduction**

55 There are two main types of Precambrian orogens: (i) accretionary and (ii) collisional
56 orogens (Windley, 1992). Accretionary orogens are wide, made up essentially of
57 juvenile crust (i.e., mantle melts with short crustal residence time) emplaced over
58 protracted periods (>60 My) of convergent deformation (Chardon et al., 2009). The
59 Svecofennian orogen (Finland, Sweden) or the Arabo-Nubian shield (NE Africa and
60 Arabia) are typical examples of Proterozoic accretionary orogens (Windley, 1992). By
61 contrast, collisional orogens are narrower belts that absorb convergence at the contact of
62 two stiff continents (e.g., the Alpine orogenic system). Their contribution to continental
63 growth is negligible because their moderate magmatism mostly reworks a crust
64 thickened by thrusting, with little magmatic input from the mantle.

65 Accretionary orogens form around stabilized continental nuclei (cratons) and are
66 the main contributor to continental growth by outward growth of continental masses
67 (e.g., Condie, 2007; Whitmeyer and Karlstrom, 2007). Contact zones between
68 accretionary orogens and their adjoining cratons are considered to be produced by the
69 collision of exotic juvenile terranes such as arcs against cratons (Cawood et al., 2006).
70 Based on the example of the southern West African Craton (sWAC), the present
71 contribution investigates the mountain building processes in such collision zones, their
72 relations to the deformation of their flanking accretionary orogen and craton, as well as
73 their role in continental growth processes.

74 The sWAC exposes a large segment of the 2.2-2.0 Ga Eburnean orogen - one of
75 the main accretionary orogens in Earth history. That segment stretches from the Guiana
76 shield of South America (where the Eburnean is termed “Transamazonian”) to
77 northwesternmost Africa (Fig. 1). In West Africa, the Eburnean orogen is made of
78 granite-greenstone terrains forming the so-called Birimian crust of the Baoulé-Mossi
79 province (Fig. 2). The orogen flanks the Sarmatia-Kénéma-Man craton (locally named
80 the Kénéma-Man province), forming the western sWAC (Wane et al., 2018). The
81 Kénéma-Man crust formed mostly around 3.6-3.5 Ga and 3.3-2.8 Ga and keeps the
82 imprint of a regional tectonothermal episode at ca. 2.8-2.7 Ga, known as the Liberian
83 event (e.g., Rollinson, 2016; Thiéblemont et al., 2004). The contact of the craton with
84 the Eburnean orogen was interpreted as a modern-like collisional orogen developed by
85 crustal-scale thrusting followed by the development of regional strike-slip shear zones
86 (Feybesse and Milési, 1994; Billa et al., 1999). In particular, low-angle crustal-scale
87 thrusts were inferred from along the periphery of the Kénéma-Man province (Fig. 2)
88 that would have transported klippen of Birimian crust onto Archean rocks. But the
89 pervasiveness of steep fabrics and strike-slip shear zones along the periphery of the
90 Kénéma-Man province and its neighboring Birimian crust instead argues for
91 transcurrent kinematics (Caby et al., 2000; Egal et al., 2002; see also Wane et al., 2018).
92 More recently, instead of collisional thrusting, HP granulites from the southeastern
93 periphery of the Archean province were suggested to result from homogeneous crustal
94 thickening of the craton margin that was reheated and softened by accretion of the
95 adjoining hot Birimian crust (Pitra et al., 2010).

96 The contentiousness of collision tectonics in the sWAC is partly due to the
97 extensive regolith cover of the area (Chardon et al., 2018), so that bedrock outcrops are

98 generally scarce or unevenly distributed, and seldom fresh or large/high enough for
99 three-dimensional structural observations. However, the area is almost entirely covered
100 by geological quadrangle maps at 1:200 000 or 1:250 000 scale that are a wealth of
101 information, especially basic structural measurements such as foliations or schistosity.

102 Here we present a mapping protocol meant to build a harmonized structural map
103 of the collision zone combining photointerpretation and the extraction of structural
104 information and measurements from the quadrangle maps. The structural map is
105 deciphered by integrating the documentation on geochronology, metamorphism and
106 field structural geology of the region. This provides a kinematic frame for collision
107 tectonics at the scale of the sWAC and the Guiana shield and allows addressing the
108 lithospheric-scale processes driving interactions between collision and crustal accretion.

109

110 **2 Methodology**

111 The regional structural pattern was obtained by mapping the tectonic fabric, which is
112 used as a regional passive strain marker (Chardon et al., 2008). This fabric has been
113 drawn by combining (i) the structural grain underlined by the lithofabrics and (ii) field
114 measurements of planar strain fabrics (schistosity and foliation, called hereafter
115 foliation) extracted from the quadrangle maps and articles. More than 7600 foliation
116 measurements were used in this study.

117 Lithofabrics were retrieved from two sources. A first type of lithofabric was
118 extracted from the quadrangle maps by drawing from lines of elongate rock bodies or
119 layers (Figs. 3a and 3b). They are called hereafter geological lithofabrics. The second
120 type of lithofabric was drawn manually by photointerpretation using the GoogleEarth™
121 software (Figs. 3c and 3d). They are called hereafter photointerpreted lithofabrics.

122 Interpretation of satellite images is relevant to map lithofabrics in basement terrains
123 based on the radiometric contrasts among lithologies (e.g., Martelat et al., 2000;
124 Chardon et al., 2008). That approach proved to be valid in the southwestern sWAC
125 (Venkatakrishnan and Culver, 1989). In such regolith- and forest-dominated terrains,
126 the use of GoogleEarth enhances more efficient and acute retrieval of lithofabrics by
127 photointerpreting high-resolution satellite images coupled with the SRTM (Shuttle
128 Radar Topography Mission) digital elevation model at 90 m resolution.

129 Photointerpreted lithofabrics are the expression of structural ridges, ridge-and-
130 trough geomorphic and/or color patterns due to the juxtaposition of lithologies of
131 contrasted nature and strength. In supracrustals, the photointerpreted lithofabrics
132 underline competent layers such as quartzite and chert beds, elongate mafic bodies or,
133 more generally, a compositional layering, particularly in volcano-sedimentary rocks. In
134 granitoid and gneiss terrains, these lithofabrics correspond to mega schlieren, mafic
135 lenses and boudins, or elongate gneissic/plutonic bodies of contrasting
136 composition/color (Fig. 3). Given the lateral variations in the vegetation/regolith cover,
137 relief, rock types or the resolution of geological surveys, the two lithofabrics are
138 unevenly expressed (Fig. 4a). Mapping the lithofabrics via two independent protocols
139 therefore allows for optimizing mapping coverage.

140 Both types of lithofabrics and the foliations have almost systematically the same
141 local trend (Figs. 3 and 4a). That parallelism indicates that lithofabrics were mostly
142 transposed into foliations and are therefore rough proxies of the latter. The three types
143 of markers (the two lithofabrics and the foliations) define collectively what is called
144 hereafter the tectonic fabric. It was drawn manually as form lines best fitting the local
145 trends of the three types of markers (Fig. 4).

146 Deciphering the asymmetrically convergent, aligning and deflection patterns of
147 the tectonic fabric allows for the identification and mapping of shear zones (Martelat et
148 al., 2000; Chardon et al., 2008; Fig. 5). Convergence patterns into belts of rectilinear
149 and parallel trajectories delineate the high-strain core of shear zones (e.g., Martelat et
150 al., 2000). Very common C/S-like patterns of the tectonic fabric further allowed for the
151 mapping of discrete map-scale shear zones (Fig. 5) as originally shown over the C/S
152 fabrics type-area (Berthé et al., 1980).

153 Our mapping protocol contributes to constraining the map trace of regional shear
154 zones that were mapped incompletely on the sole basis of geological mapping (Fig. 6).
155 This applies for instance to the Sassandra shear zone (the longest N-S feature in Fig. 6)
156 and its northern splays, as well as to the shear zones mapped West of 7°W and South of
157 8°N; Fig. 6). The method is therefore reliable to harmonize shear zone patterns by
158 enhancing the continuity of known shear zones across regolith-covered areas and to
159 detect unsuspected shear zones. The approach also allows disregarding most of the
160 minor faults (of no or limited displacement) reported on geological maps, mainly from
161 aerial photographs interpretation (Fig. 6b). These are indeed mostly fractures with no
162 relation to the ductile fabric pattern of the sWAC and are mostly linked to the rifting of
163 the Central and Equatorial Atlantic Oceans (Venkatakrishnan and Culver, 1989; Ye et
164 al., 2017).

165 Our method reveals the continuity, kinematic coherency and connectivity of
166 shear zone networks, which are anastomosed (Fig. 5). Such shear zone patterns are
167 comparable to those mapped after tectonic fabrics retrieved from aeromagnetic data
168 (Jessell et al., 2012; Chardon et al., 2020) or by combining geological surveys with
169 airborne geophysics in other parts of the sWAC (e.g., Baratoux et al., 2011; Metelka et

170 al. 2011; McFarlane et al., 2019; Mériaud et al., 2020). The resulting fabric-shear zone
171 map of the collision zone is shown in Figure 7. Higher-resolution maps showing the
172 relations between field fabric measurements and mapped shear zones are provided for
173 key areas (Figs. 8, 9 and 10), further attesting to the validity of shear zone
174 interpretation. Stereoplots of fabric data (foliations and mineral-stretching lineations)
175 from selected areas are provided in Figure 11.

176

177 **3 Structural anatomy of the collision zone**

178 3.1 Overview

179 The structural pattern is characterized by curved tectonic fabric trends and shear zones
180 that are anastomosed, delimiting shear lenses with internal fabrics roughly bisecting the
181 angle between their bounding (conjugate) shear zones (Fig. 7). Such a fabric/shear zone
182 arrangement typically reflects a continuous, heterogeneous deformation pattern (Gapais
183 et al., 1987). Three orders of shear zones are identified, attesting to the self-similar
184 properties of the shear zone network (Carreras, 2001). Only first- and second-order
185 shear zones are shown in Figure 7 for clarity. First-order shear zones are several
186 hundreds of km long and delimit mega shear lenses typically 400 km long and 250 km
187 wide (numbered from 1 to 14). Second-order shear zones are shorter (<250 km),
188 forming shear lenses ~ 200-km-long and 50-km-wide. The longest, widest and most
189 continuous first-order shear zones (Sassandra, Man-Gbanka, Kankan-Odienné and
190 Ferké) delimit large structural domains (numbered from I to IV), each comprising a
191 series of mega shear lenses. In other words, mapping allows for refining the sWAC's
192 first-order, anastomosed shear zone network (Chardon et al., 2020; Fig. 2).

193 As shown below, the structural domains, which are distinguished, by definition,
194 on the basis of their fabric and shear zone patterns, have also distinctive
195 magmatic/metamorphic histories. Moreover, the strike-slip component of the shear
196 zones (i.e., shear sense) deduced from the fabric deflection patterns on Figure 7
197 systematically matches reported field shear criteria. Deciphering the mapped
198 deformation pattern is therefore a reliable kinematic tool.

199

200 3.2 Main regional shear zones

201 The Sassandra shear zone trends N-S and is rectilinear over more than 700 km. The
202 high-strain core of the shear zone is the widest (15 km) over a 200-km-long segment
203 between $\sim 8^\circ$ and 10° N. It is narrower (<1 km) along its southern trace. The shear zone
204 merges with the Ferké shear zone at its southern tip (Fig. 7). The Sassandra shear zone
205 splits into three branches north of Odienné i.e., the Niandan shear zone, the northern
206 Sassandra shear zone and the Banifing shear zone (Liégeois et al., 1991; Pothin, 1993;
207 Caby et al., 2000; Wane et al., 2018). The Sassandra shear zone developed under high-
208 grade metamorphic conditions (700-800 °C, 5 kbar; Caby et al., 2000) and affects a
209 2.16-2.15 Ga orthogneiss near the Mali-Côte d'Ivoire border (Feybesse et al., 2006b).
210 Regional fabric and shear zone deflection patterns along the entire length of the shear
211 zone, the systematic shallow plunge of the lineations and field shear criteria (Caby et
212 al., 2000) indicate that the Sassandra shear zone is strike-slip and sinistral (e.g., Figs. 7
213 and 9a).

214 The Man-Gbanka shear zone is ENE trending. The fabric deflection pattern
215 along its trace as well as field kinematic indicators (Kouamelan et al., 1997) show that it
216 has recorded a major dextral component of shearing (Figs. 7 and 9b). The shear zone

217 core recorded granulite facies metamorphism before retrogression (Force and Beikman,
218 1977; Force and Berge, 1977; Setz, 1977a, 1977b; Williams, 1978). High temperature is
219 attested in the shear zone during the Eburnean orogeny (2.06 Ga Pb-Pb titanite age;
220 Kouamelan et al., 1997).

221 The Kankan-Odienné shear zone coincides with a major, up to 100-km-wide
222 lens-shape plutonic belt branching onto the Sassandra shear zone (mega shear lens 7 in
223 Fig. 7). It is characterized by massive, mostly juvenile 2.10-2.08 Ga plutonism (Egal et
224 al., 2002; Eglinger et al., 2017) synkinematic with regional shearing (Egal et al., 2002).
225 Systematic fabric deflections on both sides of, and inside, the shear belt as well as
226 consistent field-based shear criteria (Egal et al., 1999a, 2002; Feybesse et al., 2004d)
227 show that it is sinistral (Figs. 7 and 10a). The shear belt consists of sinistrally
228 asymmetrical shear lenses. Dominantly steep foliations oblique on the shear zone traces
229 are also consistent with sinistral shearing and the mineral-stretching lineations have
230 variable plunges (Fig. 10a). Several segments of the shear zones network have reverse
231 sense of shear (Feybesse et al., 2004b; Egal et al., 2002). The structure, fabric pattern
232 and kinematics of the Kankan-Odienné shear belt are therefore interpreted as produced
233 by partitioned sinistral transpression (e.g., Fig. 11c). In the area where the Kankan-
234 Odienné and Sassandra shear zones merge near Odienné, mineral-stretching lineations
235 are all steep in supracrustal rocks and shallowly plunging in granitoids (Fig. 9a). This,
236 together with a perturbed foliation pattern, can be a result of the partitioning of
237 stretching between the two lithologies typical of transpressional granite-greenstone
238 terrains (e.g., Hudleston et al., 1988; Chardon and Jayananda, 2008) or to strain
239 interference between the two regional shear zones or, more probably, a combination
240 both. The Kankan-Odienné shear belt recorded granulitic metamorphic conditions (800

241 °C/6-8 kbar) before retrogression down to 450-600°C and 2-3 kbar (Feybesse et al.,
242 2004d; Lerouge et al., 2004). Cooling is contemporaneous with the late activity of the
243 shear belt, constrained by Ar-Ar amphibole and biotite ages of 2.038 and 2.030 Ga,
244 respectively (Lahondère et al., 1999b; Feybesse et al., 2004b, 2004d).

245 The Ferké shear zone trends NE. It is up to 45-km-wide and constitutes a beam
246 of parallel shear zones. Further to the NE, beyond Figure 7, the shear zone affects
247 granite-greenstone terrains as young as 2.107 Ga (U-Pb zircon dating of Mériaud et al.,
248 2020), attesting to its activity until after this date. The Ferké shear zone is among the
249 longest shear zones in the sWAC. It branches onto the Banfora-Mana shear zone near
250 Bobo Dioulasso (Chardon et al., 2020; Figs. 2 and 6). SW of Soubré (Fig. 7), the shear
251 zone formed by the juncture of the Sassandra and Ferké shear zones has been shown to
252 be sinistral (Brock et al., 1977), in agreement with the sense of slip along the Sassandra
253 shear zone.

254

255 3.3 Structural domains

256 3.3.1 Domain I: Reworked high-grade Archean crust

257 This domain represents the Archean core of the Kénéma-Man province (Kouamelan et
258 al., 1997, 2018; Koffi et al., 2020; Rollinson, 2016, 2018) that was intruded by 2.10 to
259 2.02 Ga (Birimian) plutons (Thiéblemont et al., 2001, 2004; Gouedji et al., 2014). The
260 domain is bounded by the Man-Gbanka, Sassandra and Kankan-Odienné shear zones to
261 the South, East and North, respectively (Fig. 7). It is formed by a stack of eastward-
262 convex mega shear lenses (1 to 4 in Fig. 7). This arched pattern is due to the overall
263 sinistral deflection of fabrics and shear zones into the Kankan-Odienné shear zone in the
264 North, and their dextral deflection into the Man-Gbanka shear zone in the South. In the

265 westernmost part of the domain (mega shear lens 1; Fig. 7), fabrics and shear zones
266 have a dominantly N-S to NNE trend. That trend acquires a more pronounced NE
267 direction going southwestward to become ENE and aligned with the Man-Gbanka shear
268 zone. Deformation of the southern half of domain I is characterized by a rather
269 symmetrical, NE trending, high axial ratio shear lens system, moderately to (mostly)
270 steeply dipping foliations trending at a low angle to the shear zones and variably
271 plunging lineations (Fig. 10c). Such a shear-fabric pattern reflects bulk inhomogeneous
272 shortening with a component of flattening (Gapais et al., 1987).

273 The regional deflection of the fabric-shear zone pattern across domain I from N-
274 S to ENE trending is indicative of a southwestward strain gradient into the Man-Gbanka
275 shear zone. Deflection of the regional structures of domain I into the Sassandra and
276 Kankan-Odienné shear zones is accompanied by interference features marked by fabric
277 triple points, particularly in the northern parts of mega shear lenses 2 and 3 and in mega
278 shear lens 4 (Fig. 7). These patterns appear to be due to an interplay of northeastward
279 extrusion of mega shear lenses 3 and 4 and their shortening / shearing against the
280 Sassandra and Kankan-Odienné shear zones.

281 The Touba shear zone (Fig. 7) affects 2.10-2.07 Ga granitoids (Thiéblemont et
282 al., 1999a; Feybesse et al., 2004c, 2004d) and the Simandou shear zone (Figs. 7 and
283 10b) affects Birimian supracrustal rocks, whereas the 2.10-2.02 Ga plutons have Ar-Ar
284 amphibole cooling ages of 2.04-2.02 Ga (Onstott and Dorbor, 1987; Egal et al., 1999b;
285 Lahondère et al., 1999a). Regional deformation and shear zone activity in domain I are
286 therefore Eburnean (Thiéblemont et al., 2004), with strain localization and cooling
287 along the Man-Gbanka shear zone and the Kankan-Odienné shear belt. To summarize,
288 domain I may be interpreted as a major Eburnean dextral transpressive shear belt having

289 undergone strain localization in the Man-Gbanka shear zone, with modifications due to
290 interference with sinistral slip along the Kankan-Odienné and Sassandra shear zones.

291

292 3.3.2 Domain II: Hybride high-grade crust (Archean/Birimian)

293 This domain is made of mega shear lenses 5 and 6. It is pinched out in between the
294 Man-Gbanka shear zone to the N, and the Sassandra fault - Ferké shear zones to the E
295 and SE, respectively (Fig. 7). Zircon and monazite U-Th-Pb chronometry indicates that
296 domain II is made of Archean crust (ca. 3.05 and 2.80-2.70 Ga) intruded by Birimian
297 (2.15-2.06 Ga) plutonic rocks (Kouamelan et al., 1997, 2018; Cocherie et al., 1998;
298 Koffi et al., 2020). The Cestos-Nuon shear zone marking the boundary between the two
299 mega shear lenses is transcurrent (hosting shallowly plunging lineations) and records
300 granulite facies metamorphism (Force and Beikman, 1977).

301 The two mega shear lenses share the same overall ENE to NE structural grain
302 concordant with the Man-Gbanka shear zone. Shear lens 5 shows ENE-trending second-
303 order dextral shear zones mimicking the Man-Gbanka shear zone (Fig. 7). In detail,
304 shear zones are arranged in a dextral C/S-like pattern (Fig. 8b). Foliation patterns are
305 consistent with the C/S-like pattern, and tend to become steeper approaching the Man-
306 Gbanka shear zone. The mineral-stretching lineations are shallowly plunging and trend
307 at a low angle to the shear zones (Fig. 9b). At least some of the shear zones record steep
308 reverse slip (Force and Dunbar, 1977; Force and Beikman, 1977; Thorman, 1977),
309 indicative of a transpressional component of the dextral shearing. Fabric interference
310 patterns are locally documented in between the shear zones (Fig. 7). Shallowly to
311 moderately dipping foliations trending at a high angle to the shear zones are locally
312 documented (Fig. 9b). This could suggest a fabric inheritance (i.e., folding of an early

313 foliation), fabric molding around intrusions and/or lateral stretching on shallowly
314 dipping foliations in between the shear zones (e.g., Chardon et al., 2011; Block et al.,
315 2016). In any case, the shear-fabric pattern reflects bulk inhomogeneous dextral
316 transpression being kinematically linked to dextral slip along the Man-Gbanka shear
317 zone (Fig. 11b).

318 The deformation pattern of mega shear lens 5 is at variance with the consistent,
319 dense, and rectilinear fabric pattern of mega shear lens 6, which is affected by a rather
320 symmetrically anastomosed pattern of shear zones. This pattern attests to intense,
321 homogeneous and dominantly coaxial deformation in map view (Choukroune et al.,
322 1987). The Zwedru area (Fig. 6) is an exception in this pattern due to pluton
323 emplacement-related fabric interference features (Force and Beikman, 1977; Tysdal,
324 1977b). Overall, the combination of dextral slip at the northern boundary of domain II
325 (Man-Gbanka shear zone) and conjugate sinistral slip along its eastern boundary
326 (Sassandra fault) suggests that domain II escaped southwestwardly in between the two
327 shear zones.

328 Mega shear lens 5 records regional amphibolite facies metamorphism (Force and
329 Beikman, 1977). Peak metamorphic conditions in domain 6 were those of high-pressure
330 granulites (850-1000° C; 13-14 kbar) before retrogression coeval with regional partial
331 melting down to 700-800°C and 7-8 kbar (Triboulet and Feybesse, 1998; Pitra et al.,
332 2010). In mega shear lens 6, regional high-grade metamorphism overlapped in time
333 with shearing, regional high-grade metamorphism and partial melting (Tysdal, 1977a).
334 Timing constraints on that tectonothermal episode are provided by titanite Pb-Pb data
335 (2.06 Ga; Kouamelan et al., 1997) and garnet-whole rock Sm/Nd isochrones (2.05-2.03
336 Ga, Kouamelan et al., 1997, 2018), monazite U-Th-Pb ages of 2.03 Ga being ascribed to

337 regional partial melting (Cocherie et al., 1998). The timing for Eburnean tectono-
338 metamorphism in domain II is therefore comparable to that of domain I. This, together
339 with the structural and kinematic coherency between the two domains, implies that
340 domain II belongs to the Eburnean transpressional shear belt affecting domain I, called
341 hereafter the Man-Gbanka orogen. Domain II represents a side of the orogen exposing a
342 transitional crust between the Archean Kénéma-Man and Birimian Baoulé-Mossi
343 provinces, which has undergone HT-HP metamorphism. Exhumation of HP rocks may
344 have resulted from transpressional deformation (e.g., Goscombe and Gray, 2009),
345 lateral extensional flow accompanying southwestward escape of domain II or a
346 combination of both (Chardon et al., 2011). The Cestos-Nuon shear zone would have
347 accommodated partitioning of transpressional deformation between lenses 5 and 6.

348

349 3.3.3 Domain III: High-grade Birimian crust of the Baoulé-Mossi province

350 Domain III comprises mega shear lenses 8 and 9, which contrast from their hosting
351 Birimian crust (domain IV; Fig. 7) by a fabric texture comparable to that of domain II
352 and by the fact that they are affected by high-grade metamorphism and partial melting
353 (Papon, 1973; Caby et al., 2000). They are made mostly of Birimian crust (2.16 - 2.07
354 zircon U-Pb ages; Feybesse et al., 2006a, 2006b; Wane et al., 2018) and mega shear
355 lens 8 hosts slices of Mesoarchean rocks (3.20 Ga zircon U-Pb ages; Kouamelan et al.,
356 2015). The Banifing shear zone forms the western envelop of mega lens 9 (Fig. 7). The
357 shear zone affects 2.12 - 2.00 Ga syn-kinematic granitoid plutons (in-situ U-Pb zircon
358 dating), bears mineral-stretching lineations with variable plunges and underwent late
359 right-lateral shearing (Wane et al., 2018; Liégeois et al., 1991; Feybesse et al., 2006d).
360 The dense, rectilinear and parallel fabric pattern as well as the symmetrical conjugate

361 arrangement of the second-order shear zones in both shear lenses 8 and 9 argue for a
362 dominant component of intense coaxial deformation in map view, comparable to that of
363 domain II, and particularly mega lens 6. The northwestern margin of mega lens 8 is
364 formed by the Ferké shear zone (Fig. 7) that coincides with the Hana Lobo greenstone
365 belt, recording peak temperatures of 600-700°C (Papon, 1973; Ouattara, 1998). The
366 western portion of mega lens 9 near Odienné (around 9°N; Fig. 7) has steep foliations
367 (Caby et al., 2000) and mostly strike-parallel, shallowly plunging lineations that are
368 taken at a low-angle into the Sassandra shear zone (Fig. 9a). Lenses 8 and 9 of domain
369 III are interpreted as representing a lower crustal level having undergone a deformation
370 comparable to that of domain II, and having been exhumed through the lower-grade
371 Birimian Baoulé-Mossi province.

372

373 3.3.4. Domain IV: Birimian crust

374 The domain exposes the typical granite-greenstone terrains of the Baoulé-Mossi
375 province (Fig. 2), with felsic magmatism between 2.21 and 2.00 Ga constrained mostly
376 by U-Pb geochronology (Egal et al., 1999b; Lahondère et al., 2002; Feybesse et al.,
377 2004c, 2004d; Lebrun et al., 2016; Wane et al., 2018). It comprises mega shear lenses
378 10 to 14 (Fig. 7). Mega shear lens 10 hosts relics of ca. 3.5 Ga old crust (Egal et al.,
379 1999a, 2004), probably inherited from adjoining domain I, in a same manner domain II
380 inherited from domain I. Mega shear lens 10 and the Siguri basin (mega lens 11) are
381 affected by WNW-trending sinistral shear zones replicating the Kankan-Odienné shear
382 belt (Fig. 7). The N-trending structural grain of the northern Siguri basin has recorded
383 transpression, and particularly very steep reverse faulting along the N-S trending shear
384 zones (Lebrun et al., 2017; Fig. 7). Going South, those shear zones, as well as the steep

385 N-trending foliations and the variably plunging mineral-stretching lineations are taken
386 into the NW-trending shear lens pattern flanking the Kankan-Odienné shear belt (Figs.
387 10a and 11c).

388 In the rest of domain IV (mega lenses 12 to 14), foliations are mostly steep and
389 NNE trending (Fig. 10a), consistently with the shear lens patterns (Figs. 7 and 11a).
390 Lineations are mostly strike-parallel and shallowly plunging (Fig. 11a), suggesting
391 horizontal plane strain for the shear lens pattern (Gapais et al., 1987). But steep to
392 vertical lineations are also common (e.g., Figs. 9a and 11a), attesting to vertical stretch
393 and a component of flattening compatible with transpression. Steep lineations are the
394 most common in supracrustal rocks but are also reported from granitoids (Turner et al.,
395 1993). This, together with the abundance of dip-slip movements on steep outcrop-scale
396 shear zones in domain IV (Olson et al., 1992; Feybesse et al., 2004d; Traoré et al.,
397 2016; Lebrun et al., 2017), is indicative of a transpressional shear lens system as
398 documented throughout the Eburnean orogen further to the East (Chardon et al., 2020).
399

400 **4 Interpretation**

401 4.1 Case for multiscale partitioned transpression: kinematic implications

402 Our work documents a heterogeneous transpressional Eburnean deformation pattern that
403 imprinted pervasively the eastern Sarmatia-Kénéma-Man craton and the Eburnean
404 accretionary orogen through their contact zone. Transpression is attested throughout
405 multiscale, self-similar shear lens systems by (i) dominantly steep foliations, (ii) strike-
406 parallel, shallowly plunging lineations (a few being steep), and (iii) anastomosed steep
407 shear zones recording mostly strike-slip and, to a lesser extent, dip-slip (Hudleston et
408 al., 1988; Tikoff and Teysier, 1994; Tikoff and Greene, 1997; Fig. 11). At the first-

409 order, transpression is partitioned between the regional shear zones and the mega shear
410 lenses / domains they delimit (e.g., Fig. 11), which in turn are internally affected by
411 higher-order shear lens patterns. Deformation patterns of second- and third-order shear
412 lens systems are themselves transpressional and partitioned in three dimensions among
413 the anastomosed, strike-slip (mostly) to dip-slip shear zones and internal planar-linear
414 fabrics / shear patterns of the lenses they delimitate (Gapais et al., 2005). Such
415 transpressional deformation patterns are typical of Precambrian accretionary orogens
416 (e.g., Cagnard et al., 2006; Chardon et al., 2009; Duguet et al., 2009; Harris and Bédard,
417 2014; Goscombe et al., 2019) and pervasive in the rest of the sWAC (Chardon et al.,
418 2020).

419 The heterogeneity of the collisional deformation pattern may be interpreted
420 locally as interference features due to superimposed deformation phases. But the fabric-
421 shear zone pattern must have developed over a protracted period. Its heterogeneity
422 implies spatial and temporal partitioning of transpression at various scales during long-
423 lasting interactions among shear zones (Platt and Passchier, 2016; Fossen et al., 2019;
424 Chardon et al., 2020). Besides, the connectivity of the shear zone network and the
425 mutually deflecting relationships amongst shear zones at all scales indicate that the
426 kinematic coherency of the fabric-shear zone pattern was maintained during the
427 protracted deformation history (Jones et al., 2005). All this therefore warrants a large-
428 scale kinematic interpretation of the collisional map pattern of Figure 7. More generally,
429 these considerations argue for a reappraisal of the methods to tackle deformation of
430 Precambrian high grade terrains that are overwhelmingly transpressional (Fossen et al.,
431 2019). Considering large-scale kinematics in the protracted acquisition of an integrative
432 finite structural pattern should be particularly pertinent for retrieving tectonics and

433 avoiding pitfalls of the local phase approach (Carreras, 2001; Jones et al., 2005; Fossen
434 et al., 2019; Chardon et al., 2020).

435 Considering age constraints on syn-kinematic plutonism, high-grade
436 metamorphism and high temperature cooling, the main period of overlapping activity
437 for the shear zones forming the collisional network would be roughly between 2.07 and
438 2.03 Ga, with late cooling of the Man-Gbanka orogen until ca. 2.02 Ga (Fig. 12). This
439 40-50 My long collision period overlaps with late growth of the easternmost Eburnean
440 accretionary orogen until ca. 2.00 Ga (Fig. 12).

441

442 4.2 Archean inheritance

443 Within the pervasive Eburnean collisional deformation pattern (Fig. 7), identification of
444 pristine Archean (most likely Liberian, if any) fabrics is not straightforward. Best-
445 preserved Liberian fabrics would be those trending N-S in mega lens 1 i.e., the most
446 distant from, and less deflected by, the Man-Gbanka shear zone (Fig. 7), particularly in
447 their low-grade greenstone belts (500 °C/5 kbar; Barrie and Touret, 1999). In any case,
448 Eburnean deformation of domain I did not erase the memory of Liberian granulitic
449 metamorphism as preserved in the U-Pb zircon record, for instance in charnockites and
450 gneisses of mega lenses 3 and 4 (2.91-2.70 Ga; Kouamelan et al., 1997; De Waele et al.,
451 2015; Koffi et al., 2020; Fig. 7).

452

453 4.3 Crustal architecture and kinematics

454 The Man-Gbanka orogen (Fig. 13) is a key feature of the regional deformation pattern.
455 This orogen absorbed convergent deformation at the craton margin while it was being
456 rejuvenated by its flanking accretionary orogen. The orogen consists in two main belts.

457 The first belt is a > 150 km wide corridor flanking the Man-Gbanka shear zone to the
458 North, in which the softened fringe of the Sarmatia-Kénéma-Man craton (stabilized
459 after the 2.7 Ga Liberian episode) was involved into dextral transpression (Fig. 13).
460 This deformation was contemporaneous with Birimian plutonism. In the second belt, on
461 the southern side of the Man-Gbanka shear zone, Archean crust was pervasively
462 intruded by Birimian melts and underwent intense homogeneous transpressive
463 deformation and crustal thickening recorded by HP-HT metamorphism (Pitra et al.,
464 2010; Fig. 12). The contrasted deformation and metamorphic record of a same regional
465 shearing episode on either side of the Man-Gbanka shear zone reflects two contrasted
466 mechanical behaviors. To the North, it is that of a moderately attenuated craton margin,
467 partially overprinted by collisional deformation. To the South, it is that of a cratonic
468 crust having been pervasively rejuvenated by Eburnean magmatic accretion, HT-HP
469 metamorphism and deformation. The Man-Gbanka orogen is a typical mixed-hot orogen
470 i.e., relatively narrow, made almost exclusively of soft/young crust, with a high capacity
471 of tectonic burial and exhumation (Chardon et al., 2009). But instead of recording the
472 collision of two rigid continental masses, the orogen accommodated convergence at the
473 contact between an Archean craton and a wide accretionary orogen under construction.

474 The Kankan-Odienné shear belt (Figs. 7 and 13) is also interpreted as a mixed-
475 hot collisional orogen. Besides, Eglinger et al. (2017) invoked delamination of a
476 lithospheric orogenic root to explain mantle magmatism and high-grade metamorphism
477 in the shear belt. In terms of kinematics, the Kankan-Odienné orogen is sinistral and
478 cannot be the simple continuation of the Man-Gbanka orogen, which is dextral.
479 Indentation of the Eburnean orogen by the Archean Kénéma-Man province is proposed
480 to account for the finite structural pattern. However, indentation in itself does not

481 explain the termination of the Man-Gbanka orogen against the Sassandra shear zone.
482 Some high-grade terrains from the vicinity of the Mali-Côte d'Ivoire border (e.g., lens
483 9; Figs. 7 and 13) could represent slivers of the Man-Gbanka orogen extruded at the
484 front of the indenter (Chardon et al., 2020), whereas mega shear lenses 8 and 9 (Fig. 7)
485 would belong to a series of comparable exhumed migmatitic units scattered over the
486 Baoulé-Mossi province (Block et al., 2016; Fig. 13). In any case, there is a structural
487 and kinematic coherency between deformation at the eastern periphery of the indenter
488 and the regional-scale Eburnean shear zones that root into the contact (Fig. 13). East of
489 the contact zone, these shear zones are arranged in a roughly spatially consistent
490 anastomosed shear zone network typical of accretionary orogens (Fig. 13, see also Fig.
491 2).

492

493 **5 Discussion**

494 5.1 A large-scale kinematic model

495 The kinematic model of Figure 14 satisfies three main constraints. Firstly, it accounts
496 for the termination of the Man-Gbanka orogen against the Sassandra shear zone (Figs. 7
497 and 13). Secondly, the model involves clockwise rotation of the Kénéma-Man domain
498 to explain both (i) the consistent finite sinistral slip along its entire western periphery
499 (Figs. 7 and 13) and (ii) the nearly E-W trend of the dextral Man-Gbanka shear zone
500 that contrasts with the NE trend of the regional dextral shear zones, including the
501 Burghana-Transamazonian mega shear, which marks the southeastern boundary of the
502 orogen (Chardon et al., 2020). Thirdly, to explain this rotation and provide a broader
503 kinematic framework required by the size of the collision zone, we integrated
504 Transamazonian (i.e., Eburnean) structures of the Guiana shield (Fig. 1). For that, we

505 used the transatlantic correlation of Chardon et al. (2020) (Fig. 1), which is the first one
506 to be consistent with Paleoproterozoic paleomagnetic constraints (Onstott et al., 1984)
507 and was recently tested by Antonio et al. (2021) on the basis of new paleomagnetic data
508 (see Gong et al., 2021 for a recent alternative view). The kinematic model is
509 summarized as follows.

510 A series of NE-trending dextral shear zones replicating the Burghana-
511 Transamazonian mega shear cut obliquely, bend and offset eastwardly the Archean-
512 Paleoproterozoic contact that trended roughly N-S. The Man-Gbanka transpressional
513 orogen forms along that northeastwardly sheared bend, reworking the Archean as well
514 as newly accreted Birimian crust (Figs. 13 and 14a). Amplification of northeastward
515 shearing leads to the indentation of the Birimian crust (Fig. 14b). Nucleation of the
516 Pisco-Jurua shear zone (i.e., a major N-trending sinistral shear zone conjugate to the
517 Burghana-Transamazonian mega shear) is inferred to have started at that time (Fig.
518 14b). The final stage sees the last increments of indentation and clockwise rotation of
519 the Kénéma-Man indenter (Fig. 14c). Rotation is linked to sinistral slip along the Pisco-
520 Jurua shear zone and is also achieved by sinistral slip in the Kankan-Odienné shear belt,
521 as well as activation of the Sassandra shear zone and its southward propagation (Figs.
522 14c and 14d). Rotation occurs during continuing internal deformation of the indenter.
523 Southwestward escape of the hybrid crust is expected in between the Man-Gbanka shear
524 zone and the sinistral Sassandra fault that merged with the Southern Ferké shear zone.
525 Ultimately, late indentation combined with rotation of the Kénéma-Man domain leads
526 to a northward-fanning pattern of shear zones all rooted into the Sassandra shear zone
527 (Fig. 14d). That shear pattern accommodates overall northward extrusion of Birimian
528 crust north of the Archean-Birimian contact zone. The regionally anastomosed shear

529 zone system of the accretionary orogen to the east of the collision zone accommodated
530 general flow of the crust escaping northeastward (Fig. 14c).

531 To summarize, the Man-Gbanga orogen would be restricted to the sheared, NE-
532 trending portion of the Archean cratonic margin. Oblique tearing apart in that shear
533 corridor could have triggered crust-mantle connections that favored a Birimian
534 magmatic burst at the craton contact, which in turn initiated focused mixed-hot orogeny
535 along the craton margin.

536

537 5.2 Implications for Precambrian orogenic and continental growth processes

538 Convergence throughout the Eburnean accretionary orogen and its adjoining craton
539 edge was absorbed by a heterogeneous transpressional deformation pattern. The
540 Archean-Paleoproterozoic boundary in the sWAC is therefore not a collisional orogen
541 in the modern sense of the term i.e., built by the piling up of (cold) low-angle crustal-
542 scale thrust slices in between two stiff continental blocks. Such thrusts and associated
543 crustal-scale klippen would be elusive in this context of pervasive steep transpressive
544 fabrics. The Archean-Paleoproterozoic contact zone is occupied by transpressional
545 mixed-hot orogens such as the Man-Gbanka and Kankan-Odienné orogens. As opposed
546 to crustal-scale thrust sheets or nappes, displacements in these orogens were partitioned
547 among strike-slip shearing, lateral flow and vertical stretching and extrusion.

548 The metacratonization concept (Liégeois et al., 2013) was used by Wane et al.
549 (2018) to explain attenuation of the Archean crust during collision in the western
550 sWAC. That attenuation was ascribed to removal of the Archean lithospheric mantle
551 along regional shear zones while the cratonic lithosphere was being subducted under the
552 accreting Birimian arc terranes (Wane et al., 2018). An alternative collisional model is

553 developed below that would account for the specificity of mixed hot transpressional
554 orogeny that requires focused heat and fluid advection for attenuating the Archean
555 cratonic crust at that contact. In this general model, delamination of the Archean
556 lithospheric mantle at the rear (retro-side) of an accretionary orogen provides the
557 required advection (Fig. 15).

558 Numerical experiments of long-lasting collisional orogeny produce widening hot
559 orogens as a consequence of subducting slab retreat (Ueda et al., 2012). Such orogens
560 are by definition devoid of lithospheric mantle. Their crust is exposed to upward
561 asthenospheric flow leading to massive magmatic accretion, making them type-analogs
562 of Precambrian accretionary orogens (Chardon et al., 2009). The simulations of Gray
563 and Pysklywec (2012) have shown that asthenospheric upward flow due to slab retreat
564 on the pro-side of such orogens can induce delamination of the lithospheric mantle on
565 the retro-side of the orogen (i.e., the cratonic side). Retro-delamination enhances craton-
566 ward asthenospheric flow that fills in the space widened between the down-going
567 lithospheric slab and the crust (i.e., corner flow). This creates the conditions for extreme
568 heating and mixing of Archean crust with juvenile magmas. Instead of an orogenic
569 wedge, shortening of such a weak and buoyant mix results in a steep narrow
570 transpressional orogen efficient at thickening and extruding HP-HT material (Fig. 15).

571 Retro-delamination would account for a mixing of cratonic and accreted juvenile
572 crust on the retro-side of the accretionary orogen. Protracted delamination further
573 implies that the active narrow collisional orogen is transient and migrates craton-ward
574 with delamination, resulting in a progressive craton-ward “replacement” of the cratonic
575 crust by juvenile crust. If this model is correct, a craton-ward younging pattern of
576 magmatism and an increasing cratonic crustal inheritance is expected across the

577 accretionary orogen, which appears to be the case in the sWAC (Parra-Avila et al.,
578 2017, 2018; Grenholm et al., 2019). Such a pattern is at odds with a classical model of
579 unidirectional outward continental growth, although slab retreat history (Fig. 15) would
580 still permit juvenile accretion across most of the width of the accretionary orogen.
581 Finally, the retro-delamination model implies that craton-ward migration of the collision
582 zone leads to the abandonment of relict HP/HT rocks behind, which would be
583 incorporated into the accretionary orogen.

584 Long-lived delamination at the rear of accretionary orogens could ultimately
585 lead to the destruction of their flanking cratons by “digestion” of their crust by the
586 juvenile orogenic crust and sinking of the cratonic mantle lithosphere into the
587 asthenosphere. To summarize, delamination-driven retro-growth of accretionary
588 orogens at the expense of cratons opens new perspectives onto the processes of
589 continental growth. Such orogens would indeed grow partly by reworking of cratonic
590 crust into juvenile crust instead of by the sole accretion of juvenile crust against cratons.

591

592 5.3 Methodological remark

593 The present work provides a regional structural and kinematic framework for the
594 western sWAC to be tested or further documented. The methodology we have
595 developed is a cheap but powerful predictive tectonic tool integrating existing
596 documentation and freely accessible data. Such an approach should therefore be favored
597 for exploring the large-scale structure of basement terrains, especially those poorly
598 exposed or not surveyed with airborne geophysics. That approach values information
599 and structural measurements stored in quadrangle maps that are the “sleeping beauties”
600 of basement geology because they are largely unexploited. These information and data

601 were painstakingly retrieved by generations of geologists that have worked in difficult
602 environments. The present contribution is a tribute to these colleagues.

603

604 **6 Conclusion**

605 A protocol combining photointerpretation and the extraction of structural information /
606 measurements from geological maps allowed for mapping the deformation pattern of
607 the southern West African craton. The deformation pattern recorded overall E-W
608 convergence through a heterogeneous transpressive deformation pattern imprinting both
609 the Eburnean accretionary orogen and its Archean continental buttress while the orogen
610 was being built. The craton margin, which was thermally weakened by mantle
611 advection, developed a narrow hot orogenic system typified by intense steep
612 transpressive strain leading to significant crustal thickening and HP-HT metamorphism.
613 A kinematic model is proposed that involves oblique transcurrent shearing of the craton
614 margin leading to asymmetrical indentation of the accretionary orogen. The regionally
615 anastomosed shear zone system rooted into the narrow collisional orogen
616 accommodated large-scale flow of the actively growing Eburnean orogen escaping the
617 advancing indenter. Delamination of the cratonic lithospheric mantle provides a
618 mechanism for focusing heat advection at craton edge that enhanced steep narrow
619 transpressional collisional orogeny at the rear of accretionary orogens. This model has
620 implications for continental growth through the growth of accretionary orogens at the
621 expense of their flanking cratons.

622

623 **Acknowledgements**

624 This study is a contribution of the JEAi FasoLith, supported by the IRD. It was
625 facilitated by the Programme de Formation des Formateurs (University of Bamako),
626 Campus France and the French embassy in Bamako. We are indebted to Bruno Sicard
627 for enthusiastic and efficient help in launching the project and Benjamin Sawadogo for
628 support and discussions along the course of the study. Thanks are due to Mark Jessell,
629 Lenka Baratoux, Stéphane Perrouty, Yao Augustin Koffi and Salia Coulibaly for
630 sharing geological maps of the sWAC. Earlier versions of the manuscript were
631 improved through the comments of Stéphane Perrouty, Jean-Paul Liégeois and two
632 reviewers.

633

634 **References**

- 635 Allmendinger, R.W., Cardozo, N., Fischer, D.M., 2013. Structural Geology Algorithms:
636 Vectors and Tensors. Cambridge University Press. 289 pp.
- 637 Antonio, P.Y.J., D'Agrella-Filho, M.S., Nédélec, A., Poujol, M., Sanchez, C., Dantas,
638 E.L., Dall'Agnol, R., Teixeira, M.F.B., Proietti, A., Martínez Dopico, C.I.,
639 Oliveira, D.C., Silva, F.F., Marangoanha, B., Trindade, R.I.F., 2021. New
640 constraints for paleogeographic reconstructions at ca. 1.88 Ga from
641 geochronology and paleomagnetism of the Carajás dyke swarm (eastern
642 Amazonia). *Precambrian Res.* 353, 106039.
- 643 Baratoux, L., Metelka, V., Naba, S., Jessell, M.W., Grégoire, M., Ganne, J., 2011.
644 Juvenile Paleoproterozoic crust evolution during the Eburnean orogeny (~2.2–2.0
645 Ga), western Burkina Faso. *Precambrian Res.* 191, 18–45.

646 Barrie, I.J., Touret, J.L.R., 1999. Fluid inclusion studies of gold-bearing quartz veins from
647 the Yirisen deposit, Sula Mountains greenstone belt, Masumbiri, Sierra Leone.
648 Ore Geol. Rev. 14, 203–225.

649 Berthé, D., Choukroune, P., Jegouzo, P., 1979. Orthogneiss, mylonite and non coaxial
650 deformation of granites: the example of the South Armorican Shear Zone. J.
651 Struct. Geol. 1, 31–42.

652 Billa, M., Feybesse, J.-L., Bronner, G., Lerouge, C., Milési, J.-P., Traoré, S., Diaby, S.,
653 1999. Les formations à quartzites rubanés ferrugineux des Monts Nimba et du
654 Simandou: des unités empilées tectoniquement, sur un “soubassement”
655 plutonique archéen (craton de Kénéma-Man), lors de l’orogène éburnéen. C. R.
656 Acad. Sci. Paris. 329, 287–294.

657 Block, S., Jessell, M., Aillères, L., Baratoux, L., Bruguier, O., Zeh, A., Bosch, D., Caby,
658 R., Mensah, E., 2016. Lower crust exhumation during Paleoproterozoic
659 (Eburnean) orogeny, NW Ghana, West African Craton: Interplay of coeval
660 contractional deformation and extensional gravitational collapse. Precambrian
661 Res. 274, 82–109.

662 Brock, M.R., Chidester, A.H., Baker, M.W.G., 1977. Geological map of the Harper
663 quadrangle 1:250 000 (I-780-D). U.S. Geological Survey, Liberia Geological
664 Survey.

665 Caby, R., Delor, C., Agoh, O., 2000. Lithologie, structure et métamorphisme des
666 formations birimiennes dans la région d’Odienné (Côte d’Ivoire): rôle majeur du
667 diapirisme des plutons et des décrochements en bordure du craton de Man. J. Afr.
668 Earth Sci. 30, 351–374.

669 Cagnard, F., Durrieu, N., Gapais, D., Brun, J.-P., Ehlers, C., 2006. Crustal thickening and
670 lateral flow during compression of hot lithospheres, with particular reference to
671 Precambrian times. *Terra Nova* 18, 72–78.

672 Carreras, J., 2001. Zooming on Northern Cap de Creus shear zones. *J. Struct. Geol.* 23,
673 1457–1486.

674 Cawood, P.A., Kröner, A., Pisarevsky, S., 2006. Precambrian plate tectonics: Criteria and
675 evidence. *GSA Today* 16, 4–11.

676 Chardon, D., Bamba, O., Traoré, K., 2020. Eburnean deformation pattern of Burkina Faso
677 and the tectonic significance of shear zones in the West African craton. *BSGF -*
678 *Earth Sci. Bull.* 191, 2.

679 Chardon, D., Gapais, D., Cagnard, F., 2009. Flow of ultra-hot orogens: A view from the
680 Precambrian, clues for the Phanerozoic. *Tectonophysics* 477, 105–118.

681 Chardon, D., Jayananda, M., 2008. Three-dimensional field perspective on deformation,
682 flow, and growth of the lower continental crust (Dharwar craton, India). *Tectonics*
683 27, TC002120.

684 Chardon, D., Jayananda, M., Chetty, T.R.K., Peucat, J.-J., 2008. Precambrian continental
685 strain and shear zone patterns: South Indian case. *J. Geophys. Res.* 113, B08402.

686 Chardon, D., Jayananda, M., Peucat, J.-J., 2011. Lateral constrictional flow of hot
687 orogenic crust: Insights from the Neoproterozoic of south India, geological and
688 geophysical implications for orogenic plateaux. *Geochem. Geophys. Geosyst.* 12,
689 Q02005.

690 Chardon, D., Grimaud, J.-L., Beauvais, A., Bamba, O., 2018. West African lateritic
691 pediments: Landform-regolith evolution processes and mineral exploration
692 pitfalls. *Earth Sci. Rev.* 179, 124–146.

693 Choukroune, P., Gapais, D., Merle, O., 1987. Shear criteria and structural symmetry. *J.*
694 *Struct. Geol.* 9, 525–530.

695 Cocherie, A., Legendre, O., Peucat, J.J., Kouamelan, A.N., 1998. Geochronology of
696 polygenetic monazites constrained by in situ electron microprobe Th-U-total lead
697 determination: implications for lead behaviour in monazite. *Geochim.*
698 *Cosmochim. Acta* 62, 2475–2497.

699 Condie, K.C., 2007. Accretionary orogens in space and time. *Geol. Soc. Am. Spec. Pap.*
700 200, 145–158.

701 De Waele, B., Lacorde, M., Vergara, F., Chan, G., 2015. New insights on proterozoic
702 tectonics and sedimentation along the peri-Gondwanan West African margin
703 based on zircon U–Pb SHRIMP geochronology. *Precambrian Res.* 259, 156–175.

704 Delor, C., Diaby, I., Simeon, Y., Yao, B.D., Akre, D., 1998. Carte géologique de la Côte
705 d’Ivoire à 1/200 000: Danané-Man. Direction de la Géologie.

706 Delor, C., Yao, B.D., Gadou, G., Zahari, L., Simeon, Y., Deroin, J.P., Diaby, I., 1995a.
707 Carte géologique provisoire de la Côte d’Ivoire à 1/200 000: Mankono. Direction
708 des Mines et de la Géologie.

709 Delor, C., Yao, B.D., Zahari, L., Simeon, Y., Diarra, S.A., Adou, M., Deroin, J.P., Diaby,
710 I., 1995b. Carte géologique provisoire de la Côte d’Ivoire à 1/200 000: Boundiali.
711 Direction des Mines et de la Géologie.

712 Direction de la Géologie, 1996. Carte géologique de la Côte d’Ivoire à 1/200 000: Touba.
713 Ministère des Mines et de l’Energie.

714 Doumbia, S., Pouclet, A., Kouamelan, A., Peucat, J.J., Vidal, M., Delor, C., 1998.
715 Petrogenesis of juvenile-type Birimian (Paleoproterozoic) granitoids in Central

716 Côte-d'Ivoire, West Africa: geochemistry and geochronology. *Precambrian Res.*
717 87, 33–63.

718 Duguet, M., Lin, S., Davis, D.W., Corkery, M.T., McDonald, J., 2009. Long-lived
719 transpression in the Archean Bird River greenstone belt, western Superior
720 Province, Southeastern Manitoba. *Precambrian Res.* 174, 381–407.

721 Egal, E., Lahondère, D., Costea, C.A., Diabaté, B., Diallo, A., Diallo, A.B., Diallo, S.,
722 Gaye, F., Iliescu, D., Minthé, D., 1999a. Carte Géologique de la Guinée à 1/200
723 000: Siguiri (12). Ministère des Mines, de la Géologie et de l'Environnement,
724 BRGM.

725 Egal, E., Costea, C.A., Diallo, A., Diallo, S., 1999b. Carte Géologique de la Guinée à
726 1/200 000: Faranah (18). Ministère des Mines, de la Géologie et de
727 l'Environnement, BRGM.

728 Egal, E., Thiéblemont, D., Lahondère, D., Guerrot, C., Costea, C.A., Iliescu, D., Delor,
729 C., Goujou, J.-C., Lafon, J.M., Tegye, M., Diaby, S., Kolié, P., 2002. Late
730 Eburnean granitization and tectonics along the western and northwestern margin
731 of the Archean Kénéma–Man domain (Guinea, West African Craton).
732 *Precambrian Res.* 117, 57–84.

733 Egal, E., Feybesse, J.L., Bangoura, A., Billa, M., Diaby, S., Diallo, A.B., Diallo, S.,
734 Lescuyer, J.L., Sylla, B.I., 2004. Carte géologique de la Guinée à 1/200 000:
735 Dabola-Hérémakono (17-24). Ministère des Mines, de la Géologie et de
736 l'Environnement, BRGM.

737 Eglinger, A., Thébaud, N., Zeh, A., Davis, J., Miller, J., Parra-Avila, L.A., Loucks, R.,
738 McCuaig, C., Belousova, E., 2017. New insights into the crustal growth of the
739 Paleoproterozoic margin of the Archean Kénéna-Man domain, West African

740 craton (Guinea): Implications for gold mineral system. *Precambrian Res.* 292,
741 258–289.

742 Feybesse, J.L., Milési, J.P., 1994. The Archaean/Proterozoic contact zone in West Africa:
743 a mountain belt of décollement thrusting and folding on a continental margin
744 related to 2.1 Ga convergence of Archaean cratons? *Precambrian Res.* 69, 199–
745 227.

746 Feybesse, J.L., Bangoura, A., Billa, M., Diaby, S., Diallo, A.B., Diallo, S., Lescuyer, J.L.,
747 Sylla, B.I., 2004a. Carte géologique de la Guinée à 1/200 000: Dinguiraye-Bafing-
748 Makana (11-14). Ministère des Mines, de la Géologie et de l'Environnement,
749 BRGM.

750 Feybesse, J.L., Billa, M., Costea, C.A., Diabaté, B., Diaby, S., Diallo, A., Diallo, A.B.,
751 Diallo, S., Gaye, F., Iliescu, D., Lahondère, D., Milési, J.P., Minthé, D., 2004b.
752 Carte géologique de la Guinée à 1/200 000: Kankan (19). Ministère des Mines, de
753 la Géologie et de l'Environnement, BRGM.

754 Feybesse, J.L., Bangoura, A., Barry, Y., Billa, M., Costea, C.A., Diaby, S., Diabaté, B.,
755 Diallo, A.B., Diallo, S., Gaye, F., Goujou, J.C., Iliescu, D., Lahondère, D.,
756 Lescuyer, J.L., Picot, J.C., Sall, H., Sané, H., Sylla, B.I., Thiéblemont, D., Touré,
757 J., 2004c. Carte géologique de la Guinée à 1/200 000: Kérouané (26). Ministère
758 des Mines, de la Géologie et de l'Environnement, BRGM.

759 Feybesse, J.L., Bangoura, A., Billa, M., Diaby, S., Diallo, A.B., Diallo, S., Egal, E.,
760 Lescuyer, J.L., Sylla, B.I., 2004d. Carte géologique de la Guinée à 1/500 000.
761 Ministère des Mines, de la Géologie et de l'Environnement, BRGM.

762 Feybesse, J.L., Sidibé, Y.T., Konaté, C.M., Lacomme, A., Miché, J.M., Lambert, A.,
763 Zammit, C., 2006a. Carte géologique de la République du Mali à 1/200 000:

764 Massigui (NC-29-XXIV). Ministère des Mines, de l'Energie et de l'Eau, DNGM,
765 CPG, BRGM.

766 Feybesse, J.L., Sidibé, Y.T., Konaté, C.M., Lacomme, A., Miehé, J.M., Lambert, A.,
767 Zammit, C., 2006b. Carte géologique de la République du Mali à 1/200 000:
768 Tienko (NC-29-XVII). Ministère des Mines, de l'Energie et de l'Eau, DNGM,
769 CPG, BRGM.

770 Feybesse, J.L., Sidibé, Y.T., Konaté, C.M., Lacomme, A., Miehé, J.M., Lambert, A.,
771 Zammit, C., 2006c. Carte géologique de la République du Mali à 1/200 000:
772 Tingréla (NC-29-XVIII). Ministère des Mines, de l'Energie et de l'Eau, DNGM,
773 CPG, BRGM.

774 Feybesse, J.-L., Sidibé, Y.T., Konaté, C.M., Lacomme, A., Miehé, J.-M., Lambert, A.,
775 Zammit, C., BRGM, CPG, DNGM, 2006d. Synthèse géologique du Birimien
776 malien. Ministère des Mines, de l'Energie et de l'Eau. Bamako, Mali.

777 Feybesse, J.L., Sidibé, Y.T., Konaté, C.M., Lacomme, A., Miehé, J.M., Lambert, A.,
778 Zammit, C., 2006e. Carte géologique de la République du Mali à 1/200 000:
779 Bamako Est-Dioila (ND-29-V/ND-29-VI). Ministère des Mines, de l'Energie et
780 de l'Eau, DNGM, CPG, BRGM.

781 Feybesse, J.L., Sidibé, Y.T., Konaté, C.M., Lacomme, A., Miehé, J.M., Lambert, A.,
782 Zammit, C., 2006f. Carte géologique de la République du Mali à 1/200 000:
783 Bamako Ouest (ND-29-IV). Ministère des Mines, de l'Energie et de l'Eau,
784 DNGM, CPG, BRGM.

785 Feybesse, J.L., Sidibé, Y.T., Konaté, C.M., Lacomme, A., Miehé, J.M., Lambert, A.,
786 Zammit, C., 2006g. Carte géologique de la République du Mali à 1/200 000:

787 Bougouni (NC-29-XXIII). Ministère des Mines, de l’Energie et de l’Eau, DNGM,
788 CPG, BRGM.

789 Feybesse, J.L., Sidibé, Y.T., Konaté, C.M., Lacomme, A., Miché, J.M., Lambert, A.,
790 Zammit, C., 2006h. Carte géologique de la République du Mali à 1/200 000:
791 Massigui (NC-29-XXIV). Ministère des Mines, de l’Energie et de l’Eau, DNGM,
792 CPG, BRGM.

793 Force, E.R., Beikman, H.M., 1977. Geological map of the Zwedru quadrangle 1:250 000
794 (I-777-D). U.S. Geological Survey, Liberia Geological Survey.

795 Force, E.R., Berge, W.H., 1977. Geological map of the Sanokole quadrangle 1:250 000
796 (I-774-D). U.S. Geological Survey, Liberia Geological Survey.

797 Force, E.R., Dunbar, J.D.N., 1977. Geological map of the Gbanka quadrangle 1:250 000
798 (I-776-D). U.S. Geological survey, Liberia Geological survey.

799 Fossen, H., Cavalcante, G.C.G., Pinheiro, R.V.L., Archanjo, C.J., 2019. Deformation -
800 Progressive or multiphase? *J. Struct. Geol.* 125, 82–99.

801 Gapais, D., Bale, P., Choukroune, P., Cobbold, P.R., Mahjoub, Y., Marquer, D., 1987.
802 Bulk kinematics from shear zone patterns: some field examples. *J. Struct. Geol.*
803 9, 635–646.

804 Gapais, D., Potrel, A., Machado, N., Hallot, E., 2005. Kinematics of long-lasting
805 Paleoproterozoic transpression within the Thompson Nickel Belt, Manitoba,
806 Canada. *Tectonics* 24, TC3002.

807 Gong, Z., Evans, D.A.D., Youbi, N., Ait Lahna, A., Söderlund, U., Ait Malek, M.A.,
808 Wen, B., Jing, X., Ding, J., Boumehdi, M.A., Ersnt, R.E., 2021. Reorienting the
809 West African craton in Paleoproterozoic-Mesoproterozoic supercontinent Nuna.
810 *Geology* 49, 1171-1176.

- 811 Goscombe, B. D., Gray, D.R., 2009. Metamorphic response in orogens of different
812 obliquity, scale and geometry. *Gondwana Res.* 15, 151–167.
- 813 Goscombe, B., Foster, D.A., Blewett, R., Czarnota, K., Wade, B., Groenewald, B., Gray,
814 D., 2019. Neoproterozoic metamorphic evolution of the Yilgarn Craton: A record of
815 subduction, accretion, extension and lithospheric delamination. *Precambrian Res.*
816 335, 105441.
- 817 Gouedji, F., Picard, C., Coulibaly, Y., Audet, M.A., Auge, T., Goncalves, P., Paquette,
818 J.L., Ouattara, N., 2014. The Samapleu mafic-ultramafic intrusion and its Ni-Cu-
819 PGE mineralization: an Eburnean (2.09 Ga) feeder dyke to the Yacouba layered
820 complex (Man Archean craton, western Ivory Coast). *Bull. Soc. Géol. Fr.* 185,
821 393–411.
- 822 Gray, R., Pysklywec, R.N., 2012. Geodynamic models of mature continental collision:
823 Evolution of an orogen from lithospheric subduction to continental
824 retreat/delamination. *J. Geophys. Res.* 117, B03408
- 825 Grenholm, M., Jessell, M., Thébaud, N., 2019. A geodynamic model for the
826 Paleoproterozoic (ca. 2.27–1.96 Ga) Birimian Orogen of the southern West
827 African Craton – Insights into an evolving accretionary-collisional orogenic
828 system. *Earth-Sci. Rev.* 192, 138–193.
- 829 Harris, L.B., Bédard, J.H., 2014. Crustal Evolution and Deformation in a Non-Plate-
830 Tectonic Archean Earth: Comparisons with Venus, in: Dilek, Y., Furnes, H.
831 (Eds.), *Evolution of Archean Crust and Early Life*. Springer pp. 215–291.
- 832 Hudleston, P.J., Schultz-Ela, D., Southwick, D.L., 1988. Transpression in an Archean
833 greenstone belt, northern Minnesota. *Can. J. Earth Sci.* 25, 1060–1068.

834 Iliescu, D., Costea, C.A., Diabaté, B., Dupuy, J.J., Gaye, F., Lahondère, D., Minthé, D.,
835 Picot, J.C., 1999. Carte géologique de la Guinée à 1/200 000: Falama-Manankoro
836 (20-21). Ministère des Mines, de la Géologie et de l'Environnement, BRGM.

837 Jessell, M.W., Amponsah, P.O., Baratoux, L., Asiedu, D.K., Loh, G.K., Ganne, J., 2012.
838 Crustal-scale transcurrent shearing in the Paleoproterozoic Sefwi-Sunyani-
839 Comoé region, West Africa. *Precambrian Res.* 212–213, 155–168.

840 Jessell, M.W., Begg, G.C., Miller, M.S., 2016. The geophysical signatures of the West
841 African Craton. *Precambrian Res.* 274, 3–24.

842 Jones, R.R., Holdsworth, R.E., McCaffrey, K.J.W., Clegg, P., Tavarnelli, E., 2005. Scale
843 dependence, strain compatibility and heterogeneity of three-dimensional
844 deformation during mountain building: a discussion. *J. Struct. Geol.* 27, 1190–
845 1204.

846 Koffi, B. G., Ouattara, G., Kouamé F. K., Deroin, J-P. 2014. Analyse des images
847 satellitales radar RSO-ERS et optique ETM+ de Landsat 7 comme outils de
848 prospection minière: application aux localités de Tiébissou et de Tienko en Côte
849 d'Ivoire (Afrique de l'Ouest). *Afr. Sci.* 10, 47 - 67.

850 Koffi, G.R.-S., Kouamelan, A.N., Allialy, M.E., Coulibaly, Y., Peucat, J.J., 2020. Re-
851 evaluation of Leonian and Liberian events in the geodynamical evolution of the
852 Man-Leo Shield (West African Craton). *Precambrian Res.* 338, 105582.

853 Kouamelan, A.N., Delor, C., Peucat, J.J., 1997. Geochronological evidence for reworking
854 of Archean terrains during the Early Proterozoic (2.1 Ga) in the western Côte
855 d'Ivoire (Man Rise-West African Craton). *Precambrian Res.* 86, 177–199.

856 Kouamelan, A.N., Djro, S.C., Allialy, M.E., Paquette, J.L., Peucat, J.J., 2015. The oldest
857 rock of Ivory Coast. *J. Afr. Earth Sci.* 103, 65–70.

858 Kouamelan, A.N., Kra, K.S.A., Djro, S.C., Paquette, J.-L., Peucat, J.-J., 2018. The
859 Logoualé Band: A large Archean crustal block in the Kenema-Man domain (Man-
860 Leo rise, West African Craton) remobilized during Eburnean orogeny (2.05 Ga).
861 *J. Afr. Earth Sci.* 148, 6–13.

862 Lahondère, D., Costea, C.A., Diabaté, B., Diallo, A., Diallo, S., Egal, E., Gaye, F., Iliescu,
863 D., Minthé, D., 1999a. Carte géologique de la Guinée à 1/200 000: Faraba (13).
864 Ministère des Mines, de la Géologie et de l'Environnement, BRGM.

865 Lahondère, D., Iliescu, D., Bah, M., Baldé, A., Barry, Y., Diabaté, B., Gaye, F., Minthé,
866 D., Sané, H., Thiéblemont, D., 1999b. Carte géologique de la Guinée à 1/200 000:
867 Damaro-Odienné (27-28). Ministère des Mines, de la Géologie et de
868 l'Environnement, BRGM.

869 Lahondère, D., Thiéblemont, D., Tegye, M., Guerrot, C., Diabate, B., 2002. First
870 evidence of early Birimian (2.21 Ga) volcanic activity in Upper Guinea: the
871 volcanics and associated rocks of the Niani suite. *J. Afr. Earth Sci.* 35, 417–431.

872 Lebrun, E., Miller, J., Thebaud, N., Ulrich, S., McCuaig, T.C., 2017. Structural controls
873 on an Orogenic Gold System: The World-Class Siguiri Gold District, Siguiri
874 Basin, Guinea, West Africa. *Econ. Geol.* 112, 73–98.

875 Lebrun, E., Thébaud, N., Miller, J., Ulrich, S., Bourget, J., Terblanche, O., 2016.
876 Geochronology and lithostratigraphy of the Siguiri district: Implications for gold
877 mineralisation in the Siguiri Basin (Guinea, West Africa). *Precambrian Res.* 274,
878 136–160.

879 Lerouge, C., Feybesse, J.L., Guerrot, C., Billa, M., Diaby, S., 2004. Reaction textures in
880 Proterozoic calcsilicates from northern Guinea: a record of the fluid evolution. *J.*
881 *Afr. Earth Sci.* 39, 105–113.

882 Liégeois, J.P., Claessens, W., Camara, D., Klerkx, J., 1991. Short-lived Eburnian orogeny
883 in southern Mali. *Geology, tectonics, U-Pb and Rb-Sr geochronology.*
884 *Precambrian Res.* 50, 111–136.

885 Liégeois, J.-P., Abdelsalam, M.G., Ennih, N., Ouabadi, A., 2013. Metacraton: Nature,
886 genesis and behavior. *Gondwana Res.* 23, 220–237.

887 Mamedov, V., Bouféév, Y., Nikitine, Y., 2010. Carte géologique de la Guinée à 1/500
888 000. Ministère des Mines et de la Géologie, Geoprospect Ltd et Université d'Etats
889 de Moscou.

890 McFarlane, H.B., Ailleres, L., Betts, P., Ganne, J., Baratoux, L., Jessell, M.W., Block, S.,
891 2019. Episodic collisional orogenesis and lower crust exhumation during the
892 Palaeoproterozoic Eburnean Orogeny: Evidence from the Sefwi Greenstone Belt,
893 West African Craton. *Precambrian Res.* 325, 88–110.

894 Martelat, J.-E., Lardeaux, J.-M., Nicollet, C., Rakotondrazafy, R., 2000. Strain pattern
895 and late Precambrian deformation history in southern Madagascar. *Precambrian*
896 *Res.* 102, 1–20.

897 Metelka, V., Baratoux, L., Naba, S., Jessell, M.W., 2011. A geophysically constrained
898 litho-structural analysis of the Eburnean greenstone belts and associated granitoid
899 domains, Burkina Faso, West Africa. *Precambrian Res.* 190, 48–69.

900 Mériaud, N., Thébaud, N., Masurel, Q., Hayman, P., Jessell, M., Kemp, A., Evans, N.J.,
901 Fisher, C.M., Scott, P.M., 2020. Lithostratigraphic evolution of the Bandamian
902 Volcanic Cycle in central Côte d'Ivoire: Insights into the late Eburnean magmatic
903 resurgence and its geodynamic implications. *Precambrian Res.* 347, 105847.

904 Olson, S.F., Diakité, K., Ott, L., Guindo, A., Ford, C.R.B., Winer, N., Hanssen, E., Lay,
905 N., Bradley, R., Pohl, D., 1992. Regional setting, structure, and descriptive

906 geology of the middle Proterozoic Syama gold deposit, Mali, West Africa. *Econ.*
907 *Geol.* 87, 310–331.

908 Onstott, T.C., Hargraves, R.B., York, D., Hall, C., 1984. Constraints on the motions of
909 South American and African Shields during the Proterozoic: I. $^{40}\text{Ar}/^{39}\text{Ar}$ and
910 paleomagnetic correlations between Venezuela and Liberia. *Geol. Soc. Am.*
911 *Bull.* 95, 1045–1054.

912 Onstott, T.C., Dorbor, J., 1987. $^{40}\text{Ar}/^{39}\text{Ar}$ and paleomagnetic results from Liberia and
913 the Precambrian APW data base for the West African Shield. *J. Afr. Earth Sci.* 6,
914 537–552.

915 Ouattara, G., 1998. Structure du batholite de Ferkessédougou (secteur de Zuénoula, Côte-
916 d'Ivoire): Implications sur l'interprétation de la géodynamique du
917 Paléoprotérozoïque d'Afrique de l'ouest à 2.1 Ga. PhD thesis, Université
918 d'Orléans. Orléans.

919 Papon, A., 1973. Géologie et minéralisations du sud-ouest de la Côte d'Ivoire: synthèse
920 des travaux de l'opération SASCA, 1962-1968. Éditions du BRGM.

921 Papon, A., Lemarchand, R., 1973. Carte géologique du Sud-Ouest de la Côte d'Ivoire à
922 1/500 000. SODEMI-BRGM.

923 Papon, A., Lemarchand, R., 1964a. Carte géologique de la Côte d'Ivoire à 1/200 000:
924 Daloa. SODEM-BRGM.

925 Papon, A., Lemarchand, R., 1964b. Carte géologique de la Côte d'Ivoire à 1/200 000:
926 Séguéla. SODEMI-BRGM.

927 Parra-Avila, L.A., Belousova, E., Fiorentini, M.L., Eglinger, A., Block, S., Miller, J.,
928 2018. Zircon Hf and O-isotope constraints on the evolution of the

929 Paleoproterozoic Baoulé-Mossi domain of the southern West African Craton.
930 Precambrian Res. 306, 174–188.

931 Parra-Avila, L.A., Kemp, A.I.S., Fiorentini, M.L., Belousova, E., Baratoux, L., Block, S.,
932 Jessell, M., Bruguier, O., Begg, G.C., Miller, J., Davis, J., McCuaig, T.C., 2017.
933 The geochronological evolution of the Paleoproterozoic Baoulé-Mossi domain of
934 the Southern West African Craton. Precambrian Res. 300, 1–27.

935 Pitra, P., Kouamelan, A.N., Ballèvre, M., Peucat, J.J., 2010. Palaeoproterozoic high-
936 pressure granulite overprint of the Archean continental crust: evidence for
937 homogeneous crustal thickening (Man Rise, Ivory Coast). J. Metam. Geol. 28,
938 41–58.

939 Platt, J.P., Passchier, C.W., 2016. Zipper junctions: A new approach to the intersections
940 of conjugate strike-slip faults. Geology 44, 795–798.

941 Pothin, K.B., 1993. Un exemple de volcanisme du Protérozoïque inférieur en Côte
942 d'Ivoire: zone de subduction ou zone de cisaillement? J. Afr. Earth Sci. 16, 437–
943 443.

944 Rollinson, H., 2018. The geochemical evolution of Archaean felsic gneisses in the West
945 African Craton in Sierra Leone. J. Afr. Earth Sci. 143, 28–39.

946 Rollinson, H., 2016. Archaean crustal evolution in West Africa: A new synthesis of the
947 Archaean geology in Sierra Leone, Liberia, Guinea and Ivory Coast. Precambrian
948 Res. 281, 1–12.

949 Setz, J.F., 1977a. Geological map of the Voinjama quadrangle 1:250 000 (I-771-D). U.S.
950 Geological Survey, Liberia Geological Survey.

951 Setz, J.F., 1977b. Geological map of the Zorzor quadrangle 1:250 000 (I-773-D). U.S.
952 Geological Survey, Liberia Geological Survey.

953 Thiéblemont, D., Delor, C., Gounjou, J.C., Théveniaut, H., Bah, M., Baldé, A., Sané, H.,
954 Kolié, P.B., Sylla, A., Barry, Y., Lacomme, A., Vidal, M., 1999a. Carte
955 Géologique de la Guinée à 1/200 000: Beyla-Touba (31-32). Ministère des Mines,
956 de la Géologie et de l'Environnement, BRGM.

957 Thiéblemont, D., Gounjou, J.C., Bah, M., Baldé, A., Sané, H., Sall, H., Souaré, S., Touré,
958 J., Delor, C., Vidal, M., Pierre, D., 1999b. Carte Géologique de la Guinée à 1/200
959 000: N'Zérékoré-Tinsou (34-33). Ministère des Mines, de la Géologie et de
960 l'Environnement, BRGM.

961 Thiéblemont, D., Delor, C., Cocherie, A., Lafon, J.M., Goujou, J.C., Baldé, A., Bah, M.,
962 Sané, H., Mark Fanning, C., 2001. A 3.5 Ga granite–gneiss basement in Guinea:
963 further evidence for early Archean accretion within the West African Craton.
964 *Precambrian Res.* 108, 179–194.

965 Thiéblemont, D., Goujou, J.C., Egal, E., Cocherie, A., Delor, C., Lafon, J.M., Fanning,
966 C.M., 2004. Archean evolution of the Leo Rise and its Eburnean reworking. *J.*
967 *Afr. Earth Sci.* 39, 97–104.

968 Thorman, C.H., 1977. Geological map of the Monrovia quadrangle 1:250 000 (I-775-D).
969 U.S. Geological survey, Liberia Geological survey.

970 Tikoff, B., Greene, D., 1997. Stretching lineations in transpressional shear zones: an
971 example from the Sierra Nevada Batholith, California. *J. Struc. Geol.* 19, 29–39.

972 Tikoff, B., Teyssier, C., 1994. Strain modeling of displacement-field partitioning in
973 transpressional orogens. *J. Struct. Geol.* 16, 1575–1588.

974 Traoré, Y.D., Siebenaller, L., Salvi, S., Béziat, D., Bouaré, M.L., 2016. Progressive gold
975 mineralization along the Syama corridor, southern Mali (West Africa). *Ore Geol.*
976 *Rev.* 78, 586–598.

- 977 Triboulet, C., Feybesse, J.L., 1998. Les metabasites birimiennes et archéennes de la
978 région de Toulepleu-Ity (Côte-d'Ivoire): des roches portées à 8 kbar (24 km) et 14
979 kbar (42 km) au Paléoprotérozoïque. *C. R. Acad. Sci. Paris.* 327, 61–66.
- 980 Turner, P., Hall, R.P., Hughes, D.J., Whalley, J.S., 1993. The sediment-dominated
981 Boundiali-Bagoé supracrustal belt and neighbouring granitic rocks, northern Côte
982 d'Ivoire, West Africa: A Tarkwaian connection? *J. Afr. Earth Sci.* 17, 1–11.
- 983 Tysdal, R.G., 1977a. Geological map of the Buchanan quadrangle 1:250 000 (I-778-D).
984 U.S. Geological Survey, Liberia Geological Survey.
- 985 Tysdal, R.G., 1977b. Geological map of the Juazohn quadrangle 1:250 000 (I-779-D).
986 U.S. Geological Survey, Liberia Geological Survey.
- 987 Tysdal, R.G., Thorman, C.H., 1983. Geological map of Liberia 1:1 000 000 (I-1480).
988 Miscellaneous investigations series, U.S. Geological Survey, Liberia Geological
989 Survey.
- 990 Ueda, K., Gerya, T.V., Burg, J.-P., 2012. Delamination in collisional orogens:
991 thermomechanical modeling. *J. Geophys. Res. Solid Earth* 117, B08202.
- 992 Venkatakrisnan, R., Culver, S.J., 1989. Tectonic fabric of Sierra Leone, West Africa:
993 implications for Mesozoic continental breakup. *J. Geol. Soc.* 146, 991–1002.
- 994 Wane, O., Liégeois, J.P., Thébaud, N., Miller, J., Metelka, V., Jessell, M., 2018. The onset
995 of the Eburnean collision with the Kénéma-Man craton evidenced by plutonic and
996 volcanosedimentary rock record of the Masssigui region, southern Mali.
997 *Precambrian Res.* 305, 444–478.
- 998 Whitmeyer, S.J., Karlstrom, K.E., 2007. Tectonic model for the Proterozoic growth of
999 North America. *Geosphere* 3, 220–259.

1000 Williams, H.R., 1978. The Archean geology of Sierra Leone. *Precambrian Res.* 6, 251–
1001 268.

1002 Windley, B., 1992. Proterozoic collisional and accretionary orogens, in Condie, K.C.
1003 (Ed.), *Proterozoic Crustal Evolution*. Elsevier, Amsterdam, pp. 419–446.

1004 Ye, J., Chardon, D., Rouby, D., Guillocheau, F., Dall’asta, M., Ferry, J.-N., Broucke, O.,
1005 2017. Paleogeographic and structural evolution of northwestern Africa and its
1006 Atlantic margins since the early Mesozoic. *Geosphere* 13, 1254-1284.

1007

1008

1009

1010

1011

1012 **Figure captions**

1013

1014 **Figure 1.** Structural map of the Eburnean-Transazonian orogen on a Transatlantic
1015 reconstruction in today's African reference frame (modified after Chardon et al., 2020).
1016 The Reguibat shield and the southern West African craton (sWAC) are the two main
1017 outcrops of the West African craton. Tectonic fabric (thin black lines) coincides with
1018 the fabric derived from joint interpretation of medium-wavelength (>30 km) Bouger
1019 gravity anomaly and magnetic data by Jessell et al. (2016), which allowed mapping the
1020 fabrics in buried basement in West Africa.

1021

1022 **Figure 2.** Structural map of the southern West African craton (after Chardon et al.,
1023 2020).

1024

1025 **Figure 3.** Illustration of the mapping protocol of the lithofabrics deduced from the
1026 structural grain of geological maps (a, b) and photointerpretation (b, c). (a) Geology of
1027 the Ziglo area. (b) Corresponding interpretative lithofabrics (geology and foliation
1028 measurements after Papon and Lemarchand, 1973). (c) Google Earth image of the
1029 Bonju area (© 2022 Maxar Technologies, © 2022 CNES / AIRBUS). (d) Corresponding
1030 interpretative lithofabrics (foliation measurements after Setz, 1977b; Thiéblemont et al.,
1031 1999b). Map frames are located on Figure 2.

1032

1033 **Figure 4.** Mapping protocol of the tectonic fabric illustrated on the Sassandra corridor
1034 (location of map frame on Fig. 2). (a) Lithofabrics and foliation measurements. (b)

1035 Interpretative tectonic fabric and foliation measurements. Field measurements are from
1036 Papon and Lemarchand (1964a, 1964b, 1973), Force and Beikman (1977), Force and
1037 Berge (1977), Tysdal (1977b), Turner et al. (1993), Delor et al. (1995a, 1995b, 1998),
1038 Direction de la Géologie (1996), Iliescu et al. (1999), Lahondère et al. (1999),
1039 Thiéblemont et al. (1999a, 1999b), Caby et al. (2000), Feybesse et al. (2006a, 2006b),
1040 Mamedov et al., (2010). International borders are shown as blue dashed lines in (a).
1041 Localities are shown on both maps as white dots.

1042

1043 **Figure 5.** Illustration of the shear zone mapping protocol. (a) Tectonic fabric. (b)
1044 Tectonic fabric and interpreted shear zones. (Same map frame and localities as in Fig.
1045 4)

1046

1047 **Figure 6.** Comparison of the shear zone pattern mapped for the present study (a) and
1048 field mapping (b) on the example of the Sassandra corridor (same map frame and
1049 localities as in Figs. 4 and 5). Supracrustals/greenstones are shown in green. (b) is
1050 compiled after Papon and Lemarchand (1964a, 1964b, 1973), Force and Beikman
1051 (1977), Force and Berge (1977), Tysdal (1977b), Delor et al. (1995a, 1995b, 1998),
1052 Direction de la Géologie (1996), Kouamelan et al. (1997), Iliescu et al. (1999),
1053 Thiéblemont et al. (1999a, 1999b), Caby et al. (2000), Feybesse et al. (2006a, 2006b),
1054 Koffi et al. (2014).

1055

1056 **Figure 7.** Structural map of the Archean-Paleoproterozoic collision zone, western
1057 portion of the southern West African craton (map frame located on Fig. 2). Mega shear
1058 lenses (separated by first-order shear zones) are numbered from 1 to 14. Our fabric

1059 mapping in the Faranah - Makeni area is complemented by that of Venkatakrishnan and
1060 Culver (1989). Inset: Main structural domains (numbered I to IV) and first-order shear
1061 zones. Wider shear zones (> 5 km) are filled in dark grey.

1062

1063 **Figure 8.** Simplified structural map of the western part of the southern West African
1064 craton (simplified from Fig. 7) showing the areas of Figures 9, 10 and 11.

1065

1066 **Figure 9.** Maps showing the relations between the mapped shear zone pattern and fabric
1067 measurements (the two maps have the same scale and orientation; location on Fig. 8).

1068 (a) Odienné quadrangle, northern portion of the Sassandra shear zone at the junction
1069 with the Kankan-Odienné shear belt (measurements after Caby et al., 2000). All the
1070 sub-vertical mineral-stretching lineations are reported from supracrustal rocks. (b)

1071 Northern half of the Gbanka quadrangle, encompassing the Man-Gbanka shear zone
1072 (measurement after Force and Dundar, 1977). Wider shear zones (Fig. 7) are filled in
1073 light grey.

1074

1075 **Figure 10.** Maps showing the relations between the mapped shear zone pattern and
1076 fabric measurements (located on Fig. 8). (a) Kankan quadrangle, northern margin of the

1077 Kankan-Odienné shear belt / southern Siguiri basin (measurements after Feybesse et al.,
1078 2004b). (b) Zorzor area, encompassing the Simandou shear zone (measurements after

1079 Stez, 1977b; Thiéblemont et al., 1999b). Wider shear zones (Fig. 7) are filled in light
1080 grey.

1081

1082 **Figure 11.** Statistics of fabric measurements for three regions of the study area where
1083 mineral-stretching lineations are documented (see Fig. 8 for the areas of data
1084 collection). (a) Eastern part of the study area, encompassing the Sassandra shear zone
1085 and eastern domain IV (mostly). (b) South-central part of the study area, encompassing
1086 the Man-Gbanka shear zone. (c) Northwestern part of the study area, encompassing the
1087 western portion of the Kankan-Odienné shear belt. Partitioning schemes depict averaged
1088 shear lens systems deduced from foliation trends maxima (red arrows) considered as
1089 tracking the two main sets of shears flanking the shear lenses. Orientation of the shear
1090 lenses is compared to that of the nearest regional scale shear zone. Equal area, lower
1091 hemisphere nets, data contoured at 2σ using the Stereonet software (Almendinger et al.,
1092 2013). Sources for the data in (a): Papon and Lemarchand (1964b); Turner et al. (1993);
1093 Delor et al. (1995a, 1995b, 1998); Direction de la Géologie (1996); Lahondère et al.
1094 (1999b); Caby et al. (2000); Feybesse et al. (2006a, 2006b, 2006c, 2006e, 2006f, 2006g,
1095 2006h); (b): Papon and Lemarchand (1973); Force and Beikman (1977); Force and
1096 Berge (1977); Force and Dunbar (1977); Setz (1977a, 1977b); Thorman (1977);
1097 Wallace (1977); Tysdal and Thorman (1983); Thiéblemont et al. (1999a, 1999b); Delor
1098 et al. (1998); Mamedov et al. (2010) and (c): Egal et al. (1999a, 1999b, 2004) ;
1099 Feybesse et al. (2004a, 2004b, 2004c); Mamedov et al. (2010).

1100

1101 **Figure 12.** Simplified time frame for Eburnean plutonism (U-Th-Pb dating), high-grade
1102 metamorphism and partial melting (U-Th-Pb dating), and high temperature cooling
1103 (amphibole and biotite Ar-Ar dating) in the Archean-Paleoproterozoic collision zone of
1104 the southern West African craton (map area of Fig. 7). Compiled after Onstott and
1105 Dorbor (1987); Cocherie et al. (1998); Kouamelan et al. (1997, 2015, 2018); Egal et al.

1106 (1999b, 2002); Lahondère et al. (1999a, 1999b, 2002); Thiéblemont et al. (1999a, 2001,
1107 2004); Feybesse et al. (2004b, 2004c, 2004d, 2006a, 2006b); Gouedji et al. (2014);
1108 Lebrun et al. (2016); Eglinger et al. (2017); Wane et al. (2018); Koffi et al. (2020);
1109 Mériaud et al. (2020).

1110

1111 **Figure 13.** Sketch structural model for the Archean-Paleoproterozoic collision in the
1112 southern West African craton. The Man-Gbanka shear zone trends NE at this stage i.e.,
1113 before clockwise rotation of the Kénéma-Man domain that led to its final ENE trend
1114 (see Fig. 14). Among the exhumed lower crustal units, those extruded at the front of the
1115 Man-Gbanka orogen may still contain relicts of Archean crust (e.g., mega shear lens 8
1116 in Fig. 7; Kouamelan et al., 2015). Others, more distant from the collision zone, would
1117 essentially be made of Birimian juvenile crust accreted after 2.23 Ga.

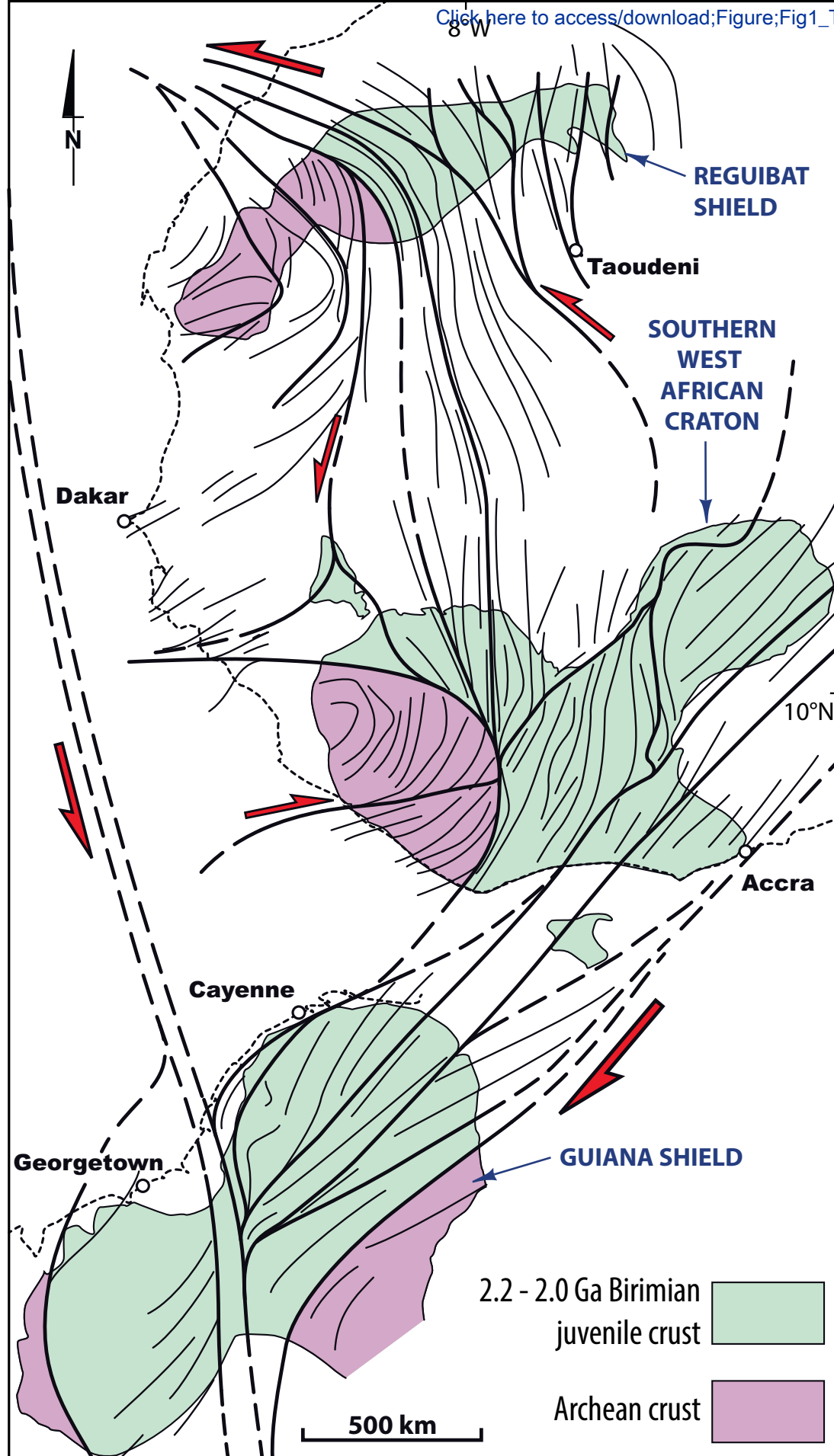
1118

1119 **Figure 14.** Kinematic model for the collision between the Sarmatia-Kénéma-Man
1120 craton and the Eburnean accretionary orogen. (a) Early, oblique shearing stage. (b)
1121 Indentation stage. (c) Late stage of indentation and clockwise rotation of the deforming
1122 indenter. (d) Sketch illustrating the rotation from stage (b) to stage (c). Shear pattern in
1123 the eastern sWAC and Guiana shield are adapted from Chardon et al. (2020).

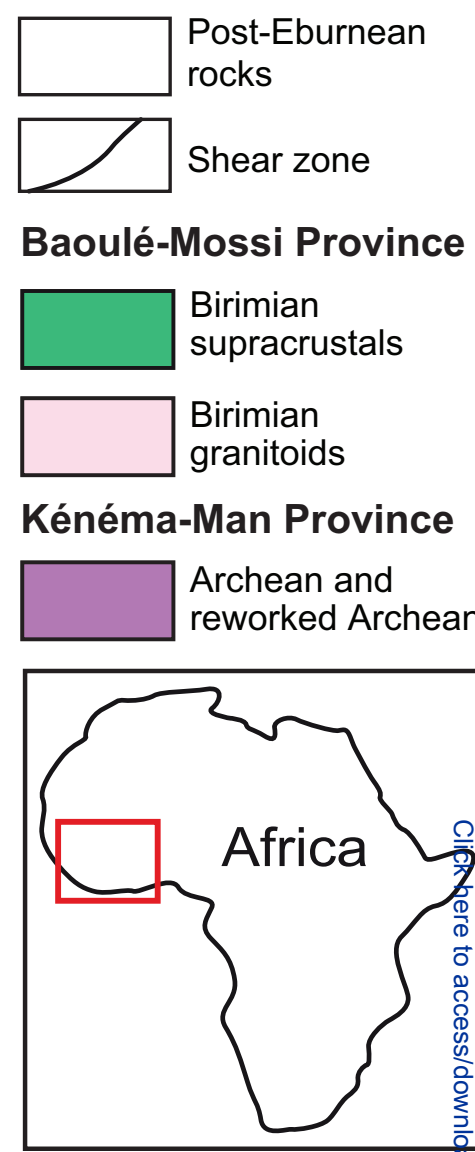
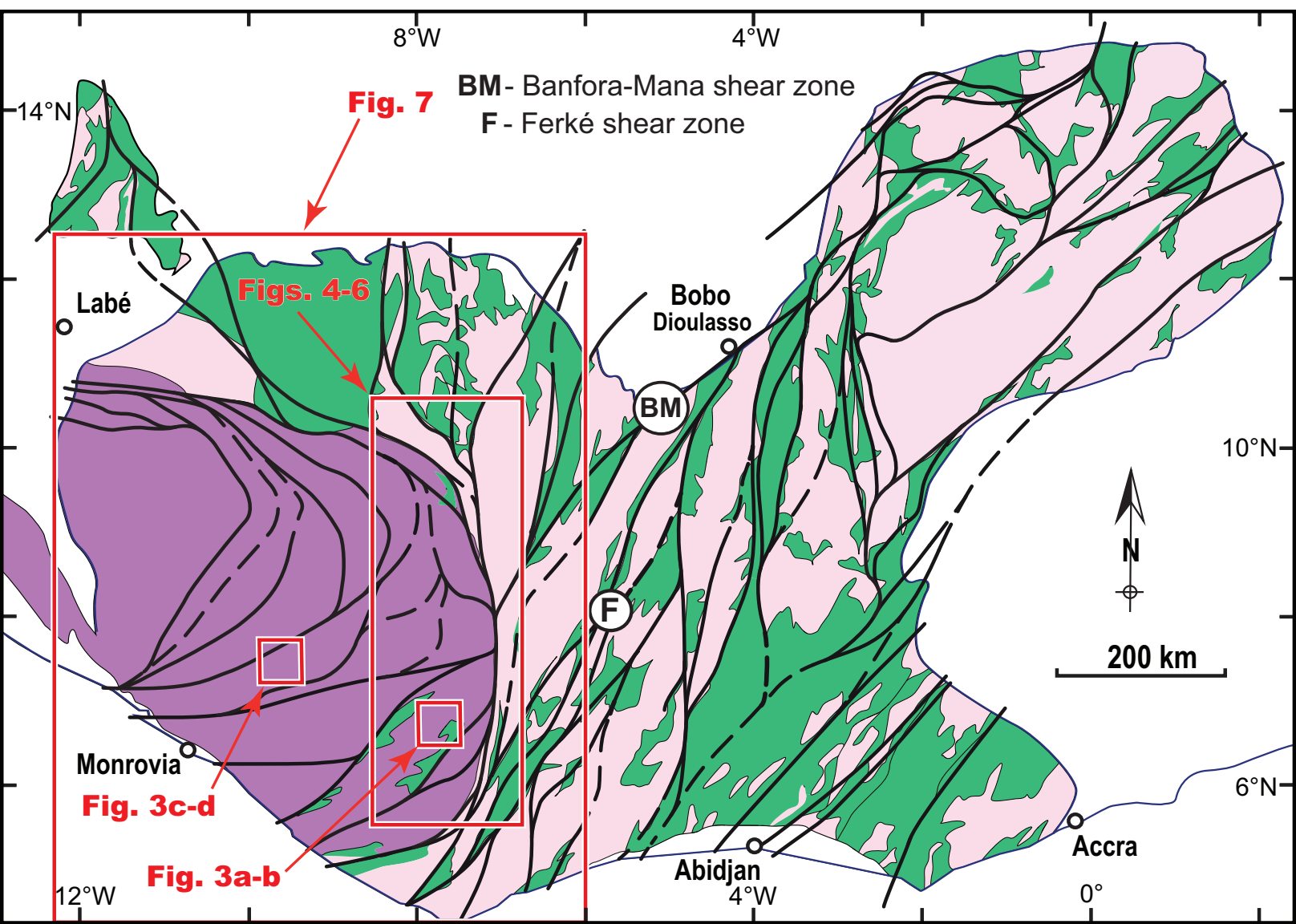
1124

1125 **Figure 15.** Lithospheric-scale configuration of collision at the contact of an
1126 accretionary orogen with its flanking craton, adapted for the present study from the
1127 models of Chardon et al. (2009) and Gray and Pysklywec (2012). Upward
1128 asthenospheric flow due to slab retreat at the pro-side of the orogen induces retro-
1129 delamination of the cratonic lithospheric mantle. This leads to hot asthenospheric corner

1130 flow - and therefore heat/magmatic advection - into the craton-accretionary orogen
1131 collision zone (e.g., the Man-Gbanka orogen in the West African case, on a broadly W-
1132 E cross-section). The collision zone therefore absorbs convergence by steep
1133 transpression and vertical extrusion of ultra-soft, HP-HT hybrid (cratonic and juvenile)
1134 crust.
1135



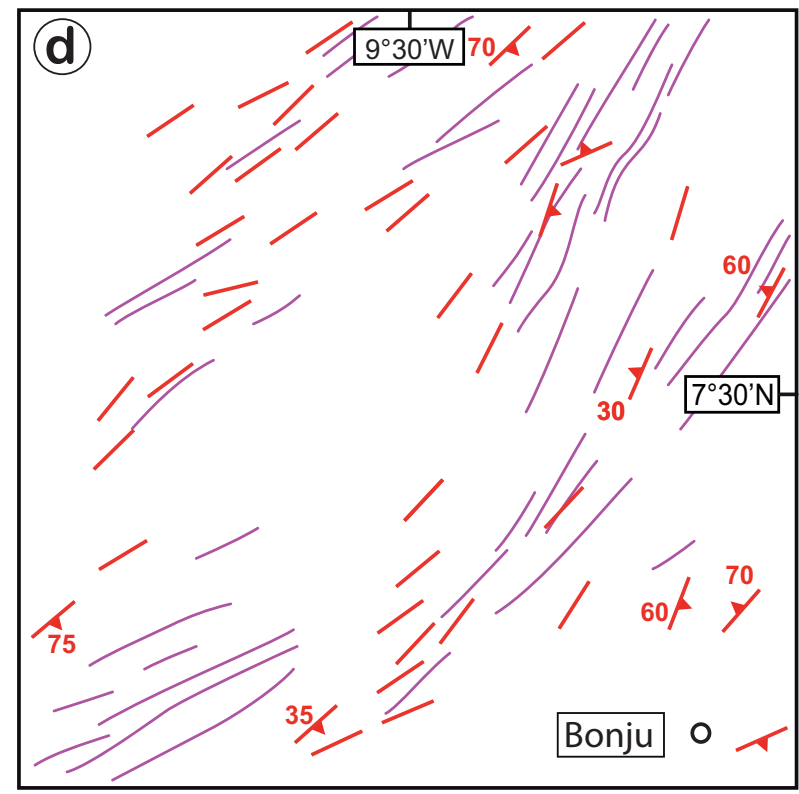
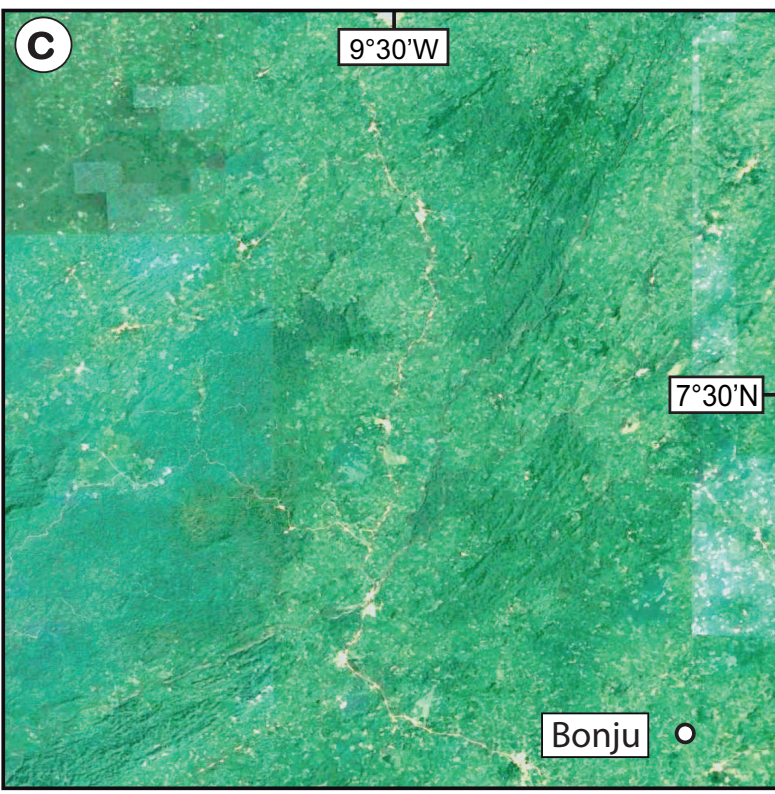
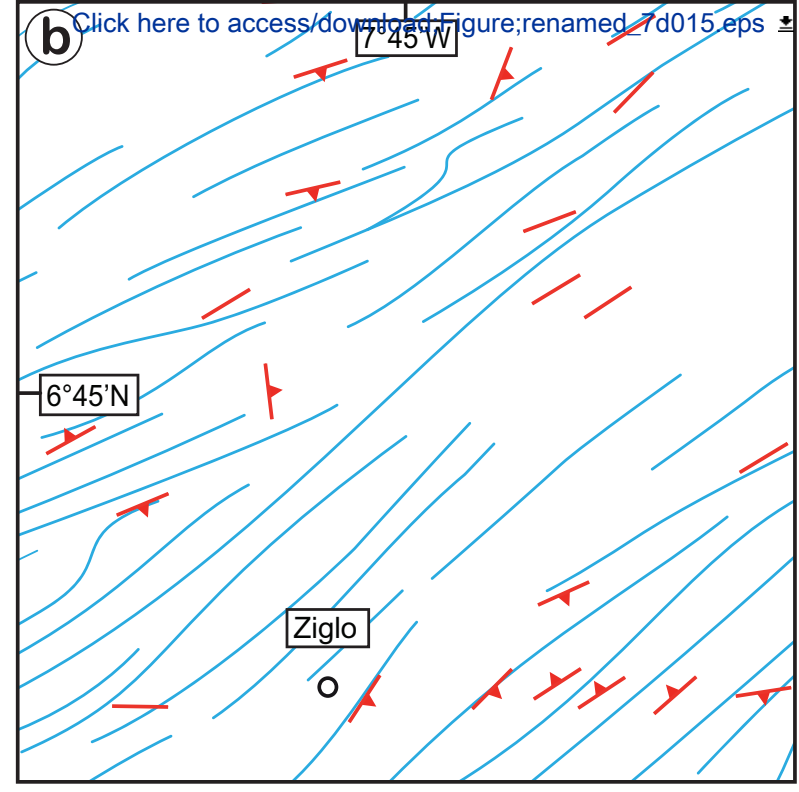
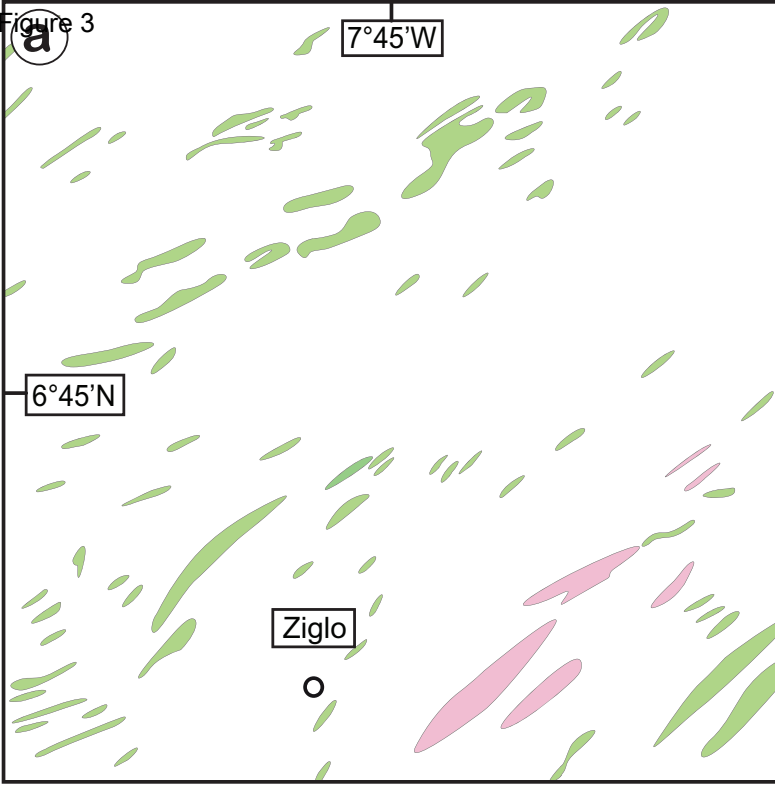
Traoré et al., Fig. 1



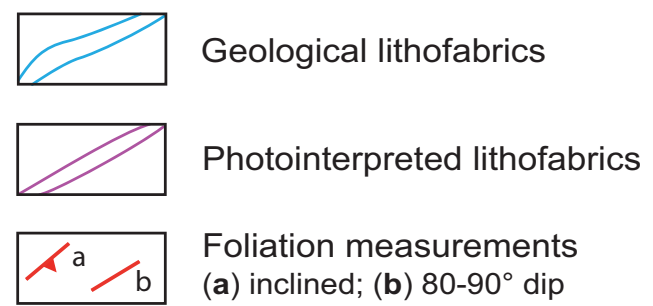
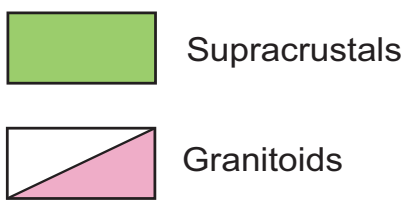
Traoré et al., Fig. 2

Figure 3

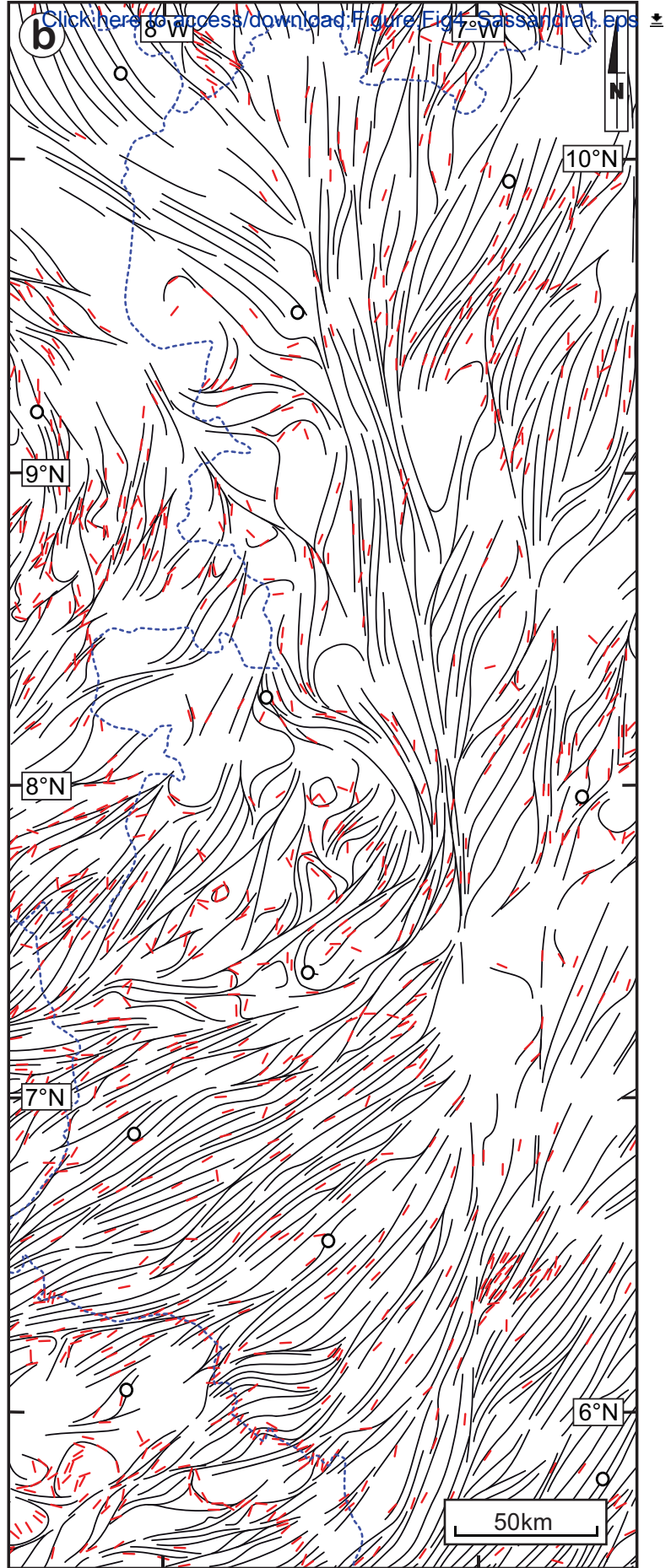
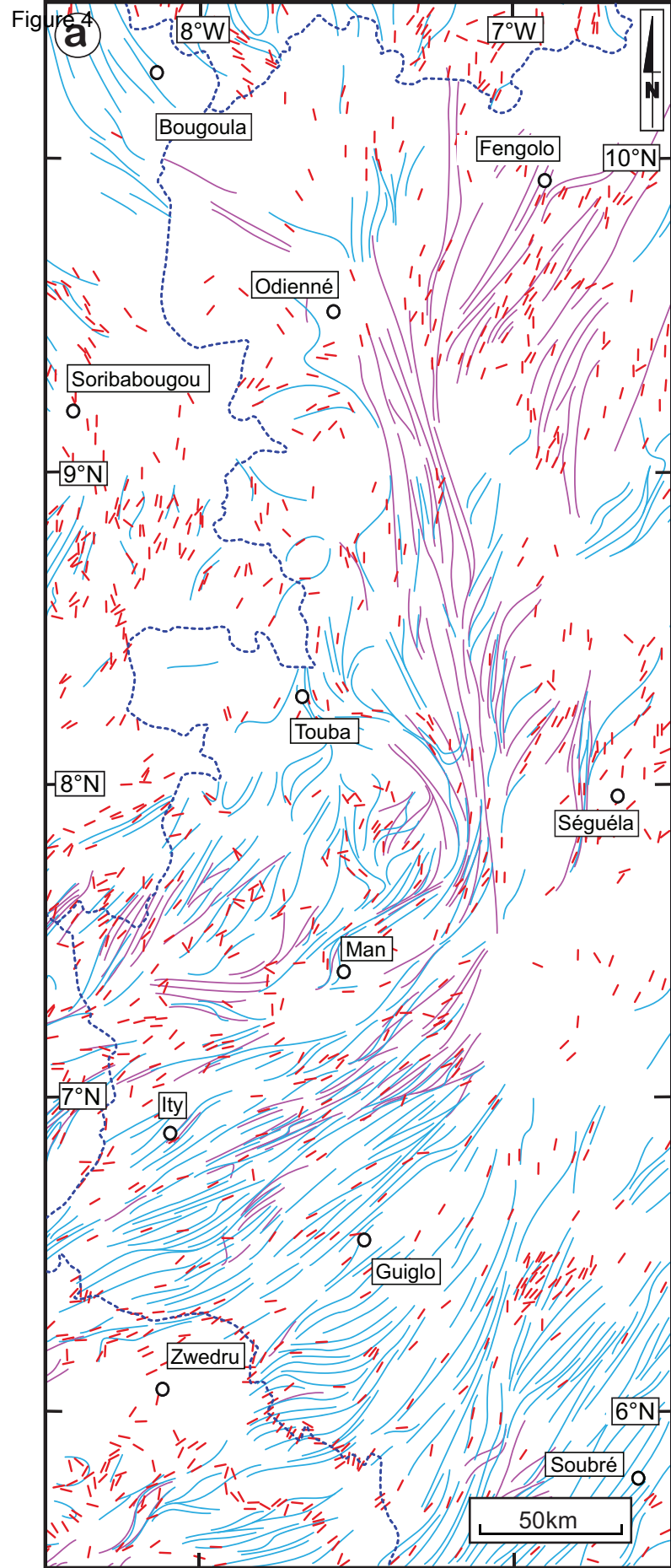
[Click here to access/download/Figure;renamed_7d015.eps](#)



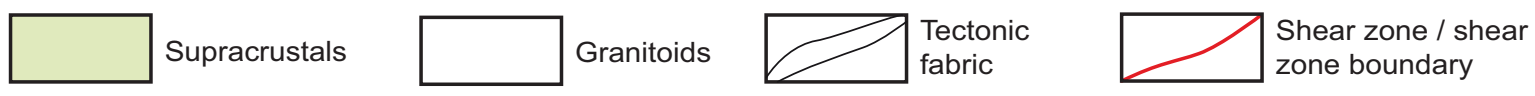
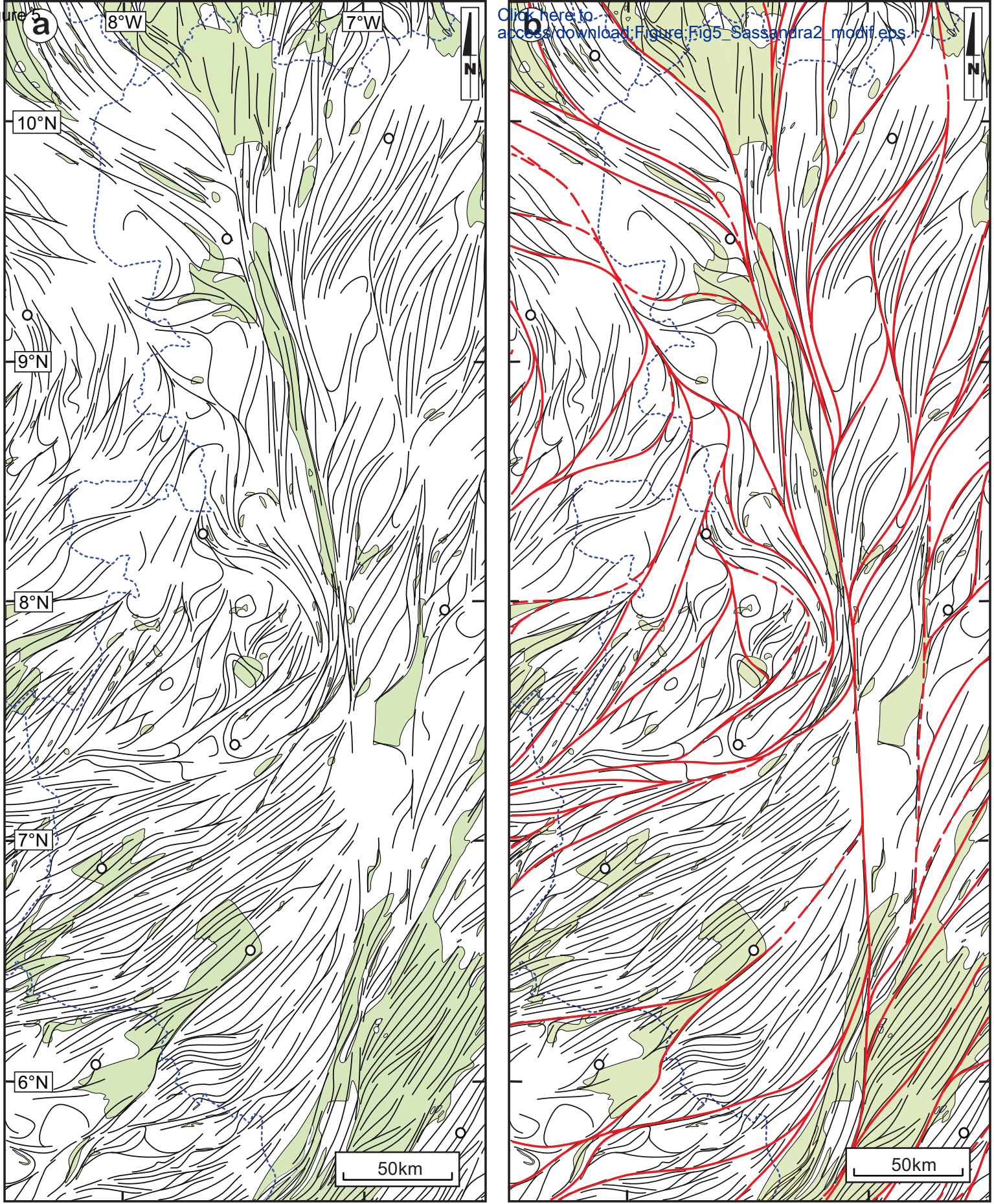
30 km



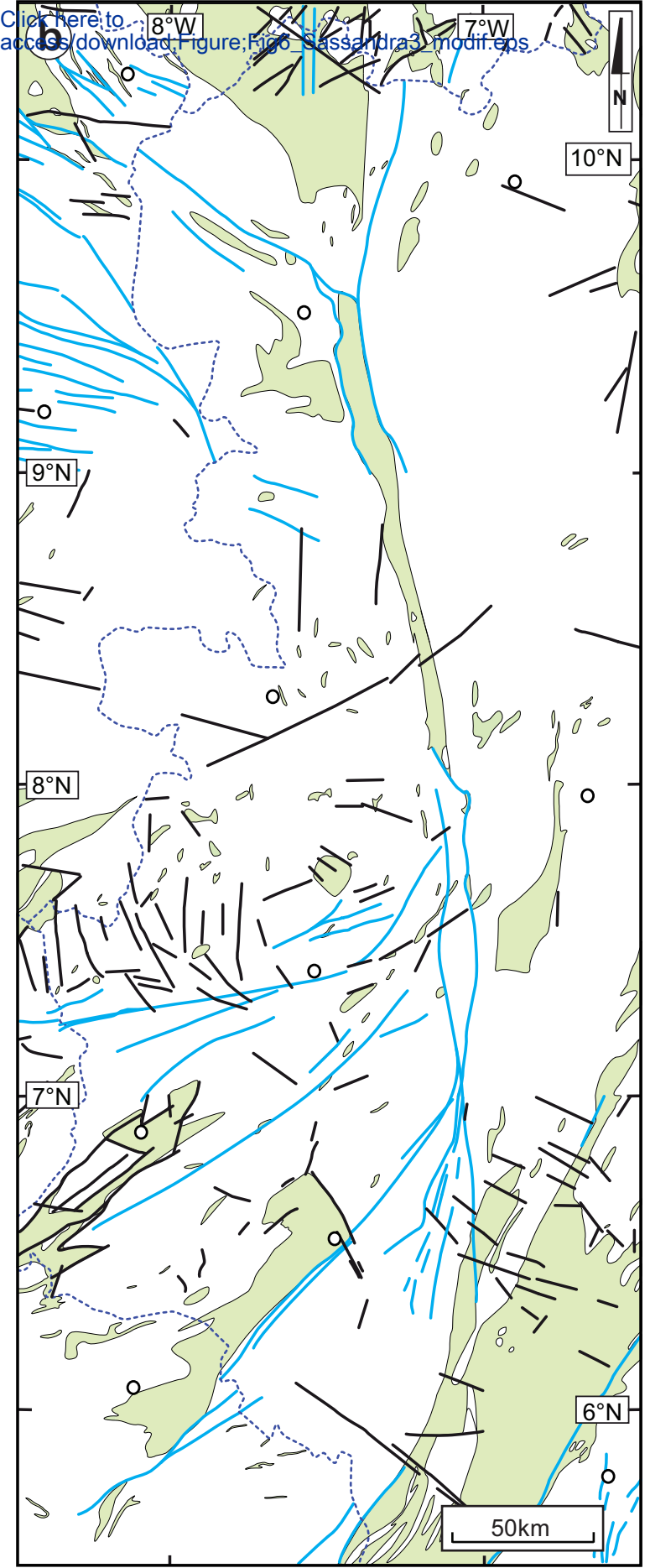
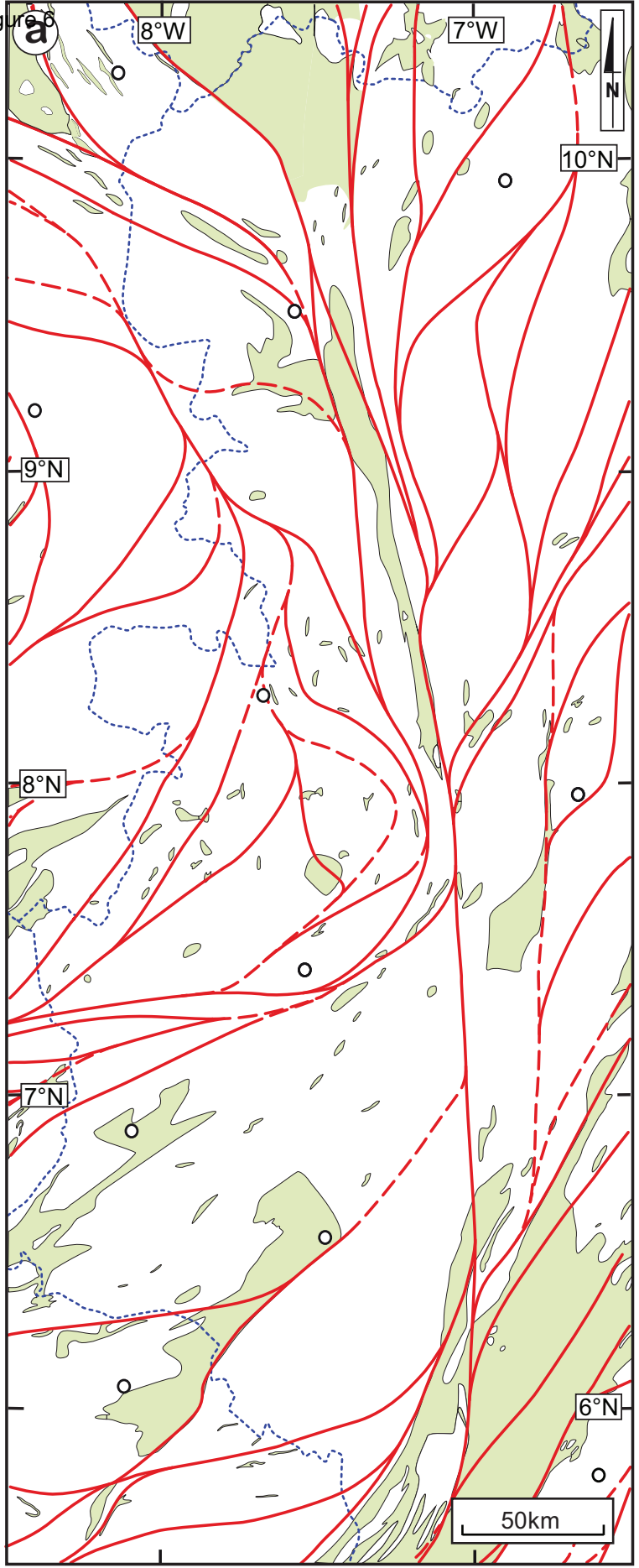
Traoré et al., Fig. 3



Traoré et al., Fig. 4



Traoré et al., Fig. 5



 Shear zone / shear zone boundary

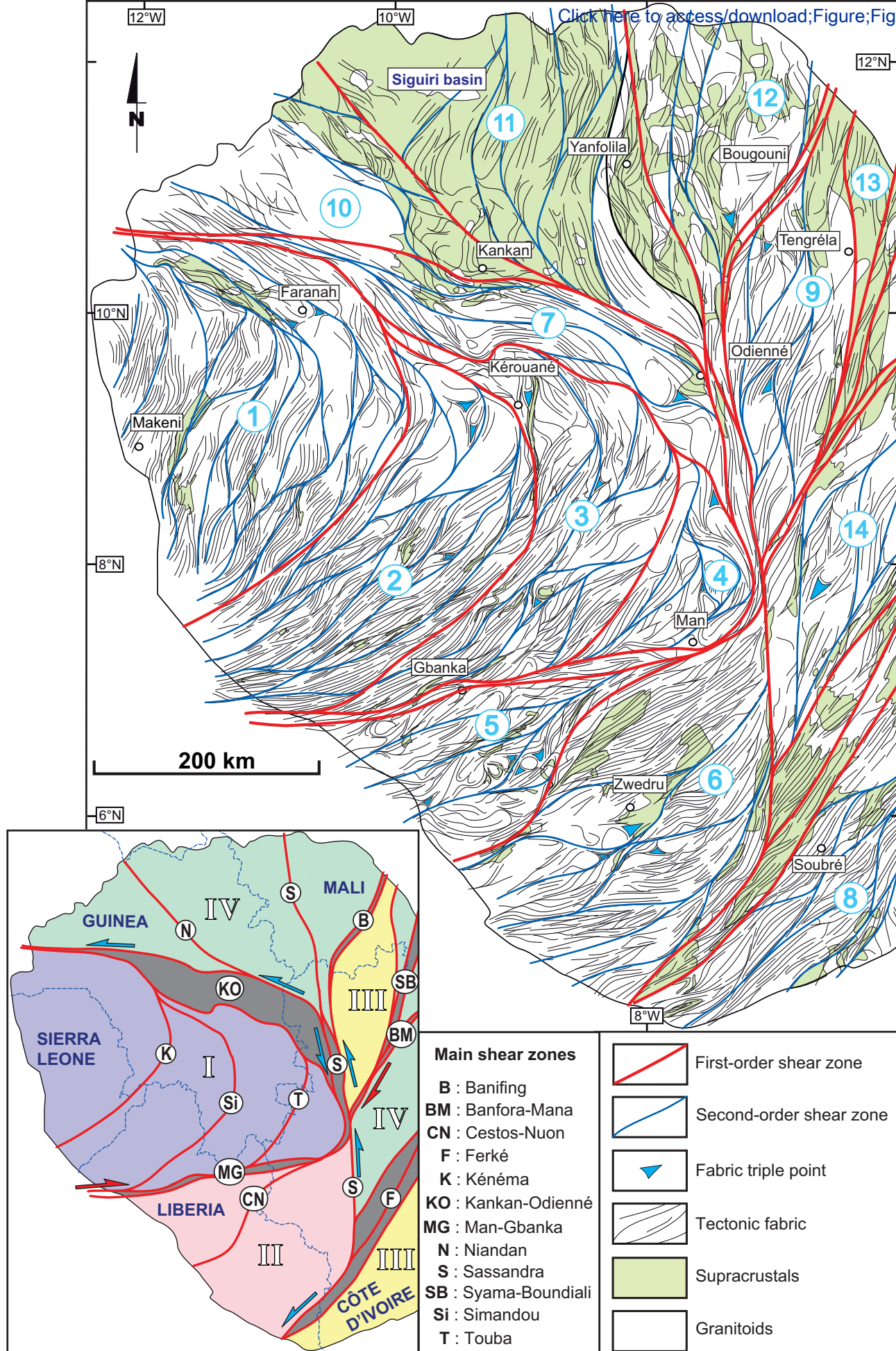
 Shear zone / shear zone boundary

 Fault

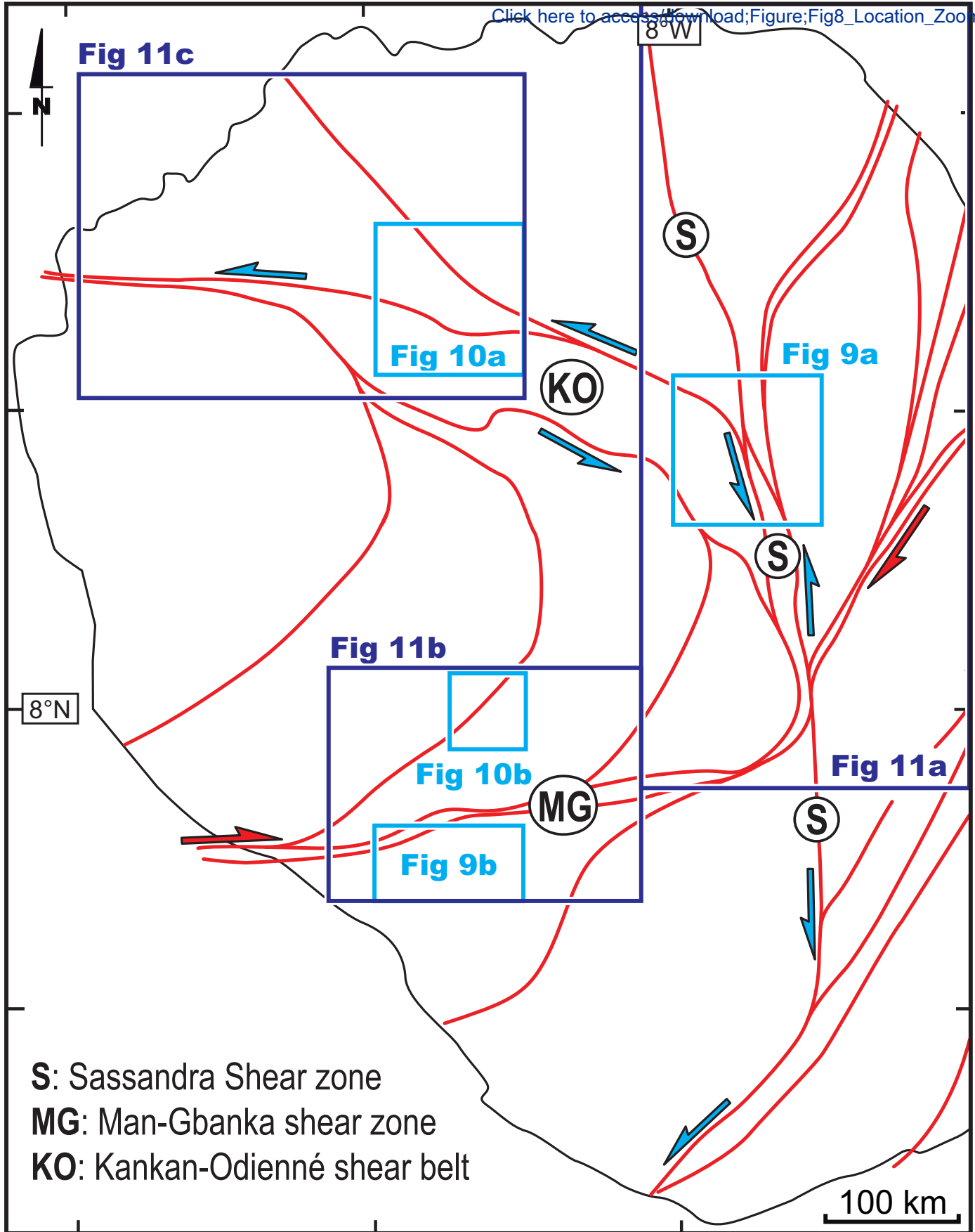
Traoré et al., Fig. 6

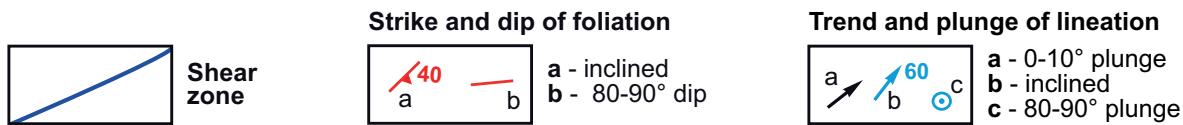
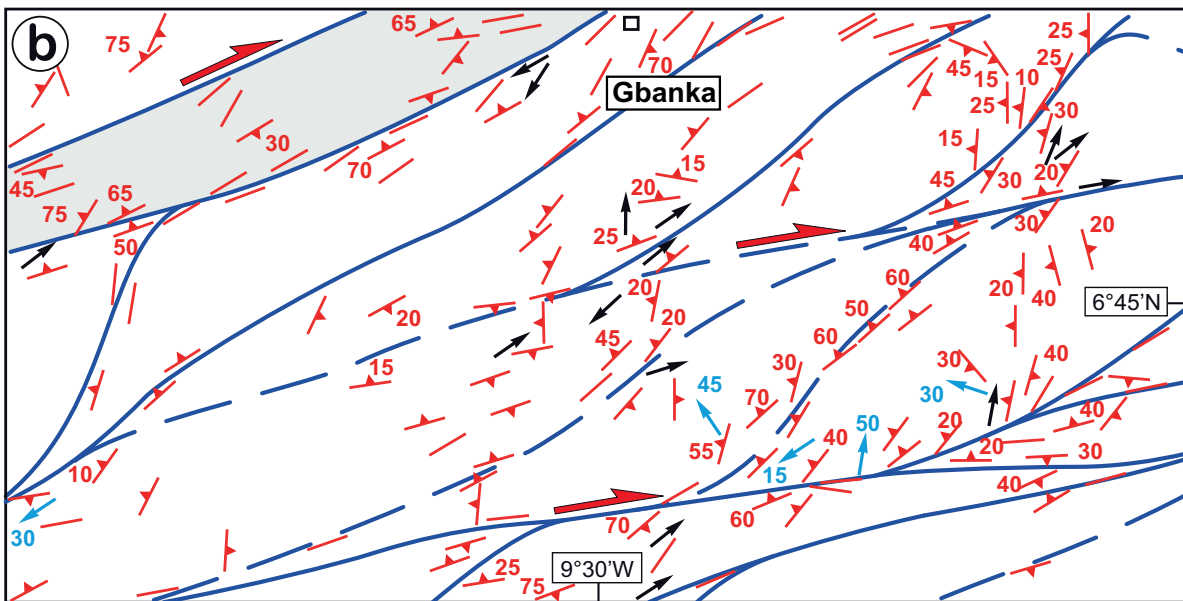
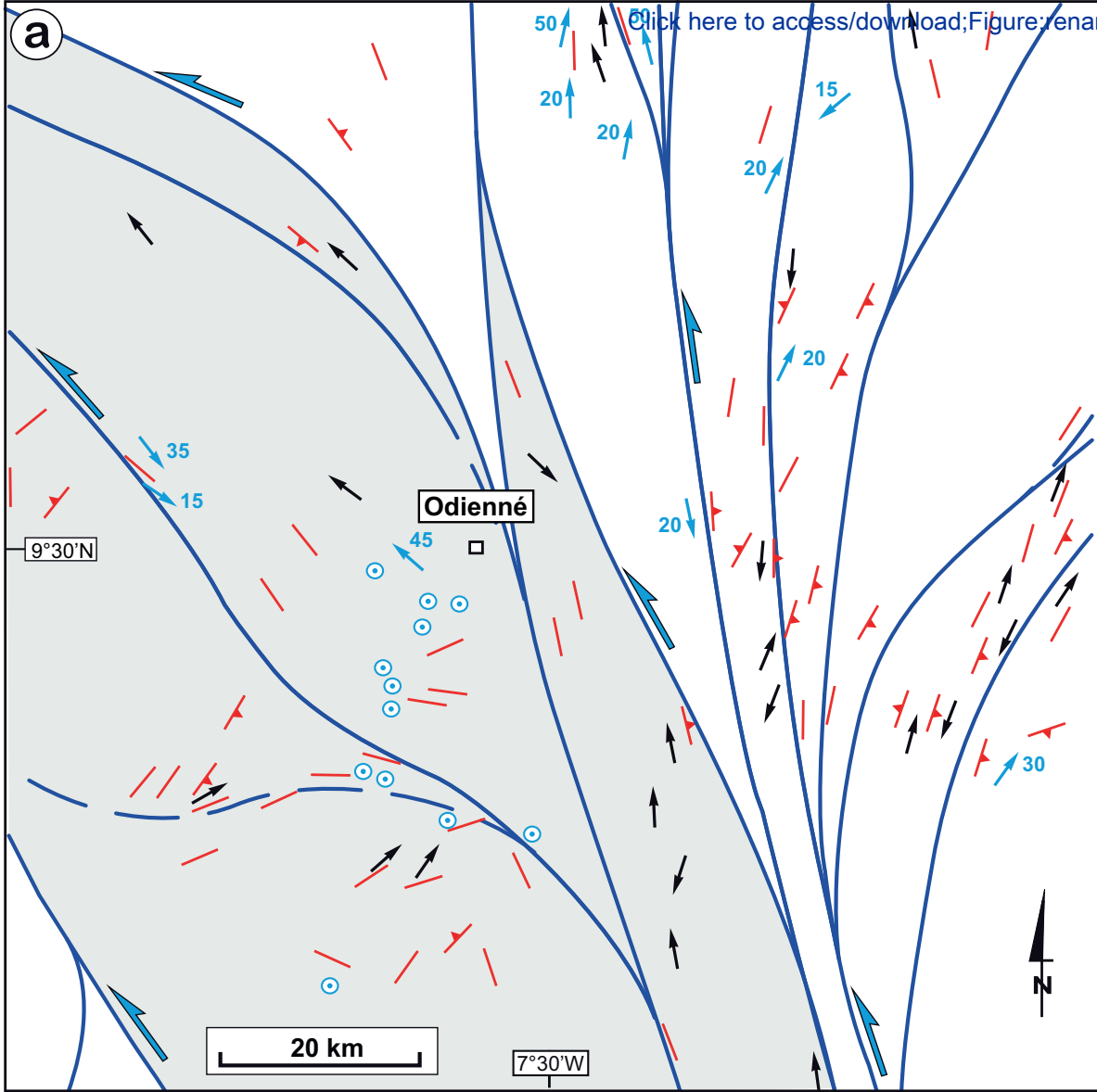
Figure 7

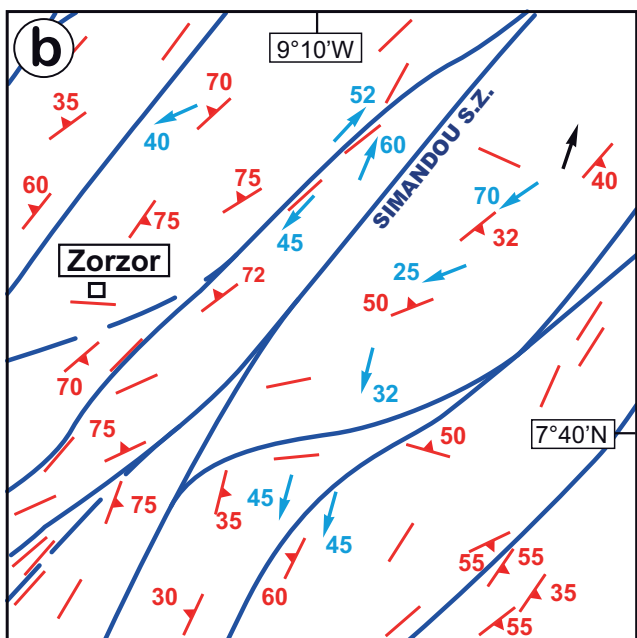
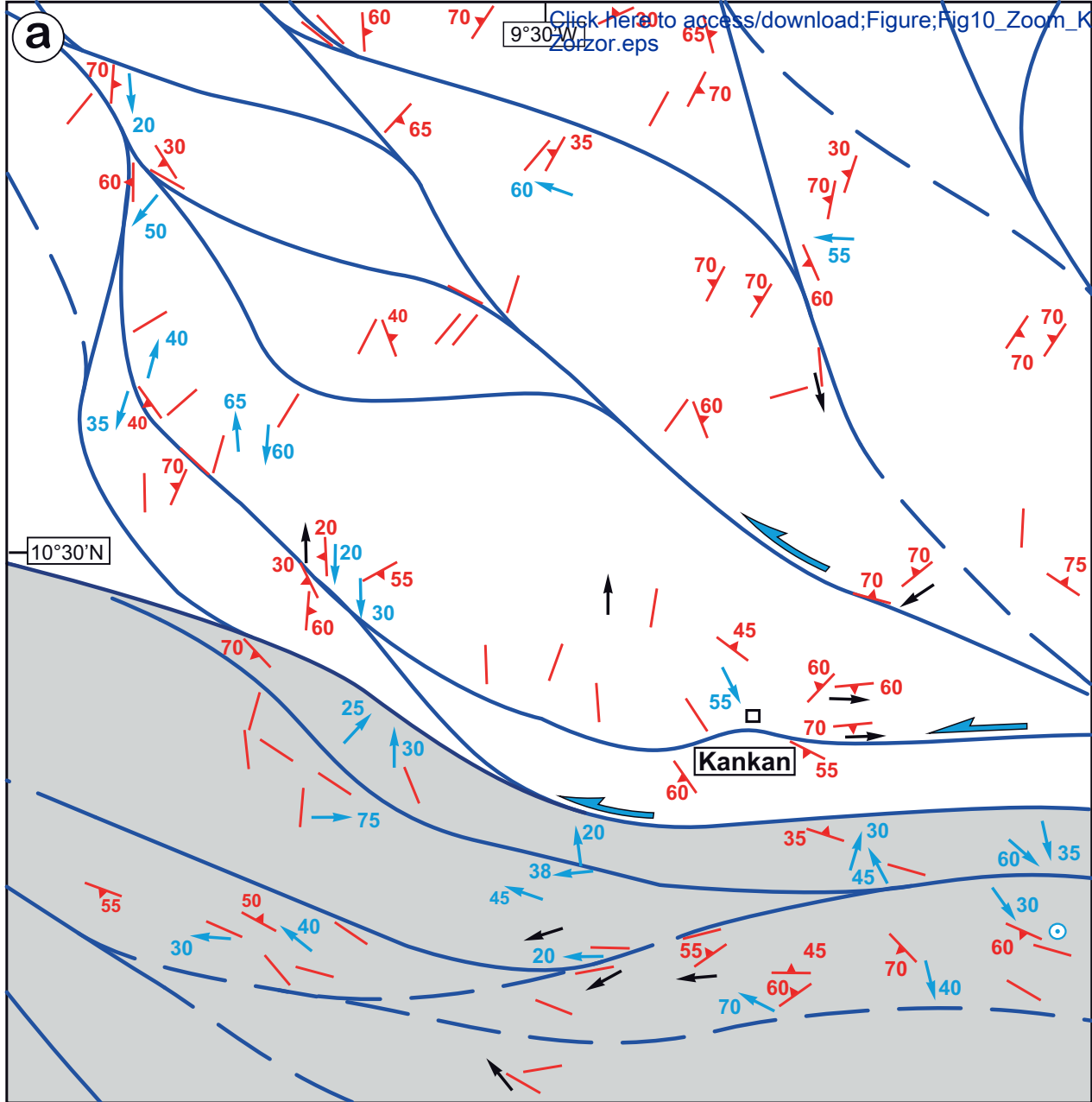
[Click here to access/download;Figure;Fig7_MAP.eps](#)



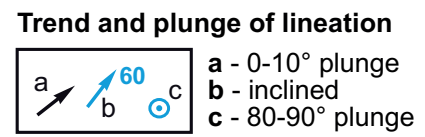
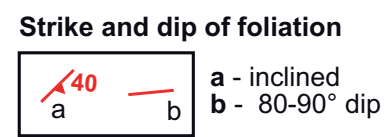
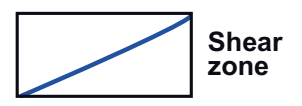
Traoré et al., Figure 7

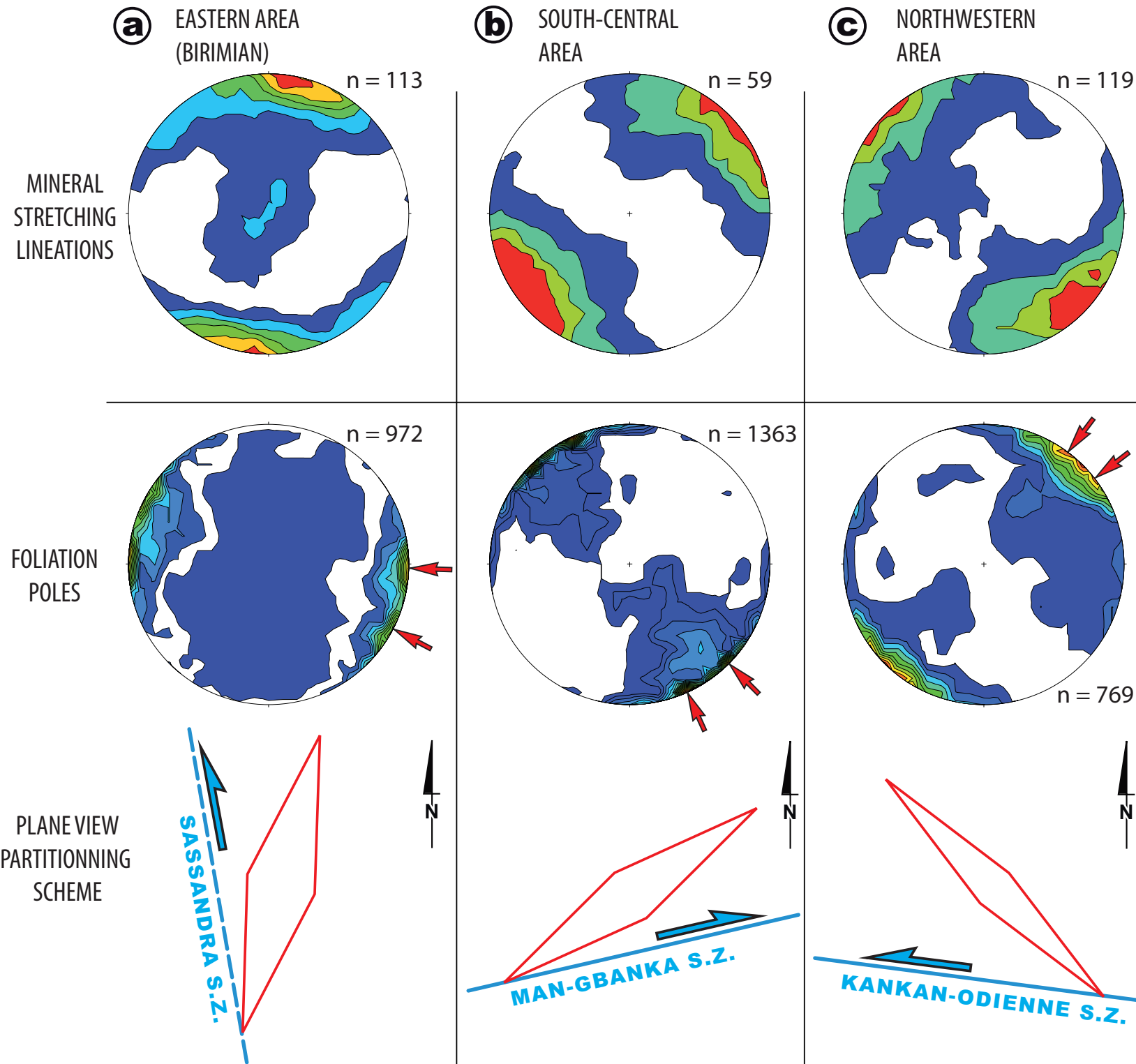




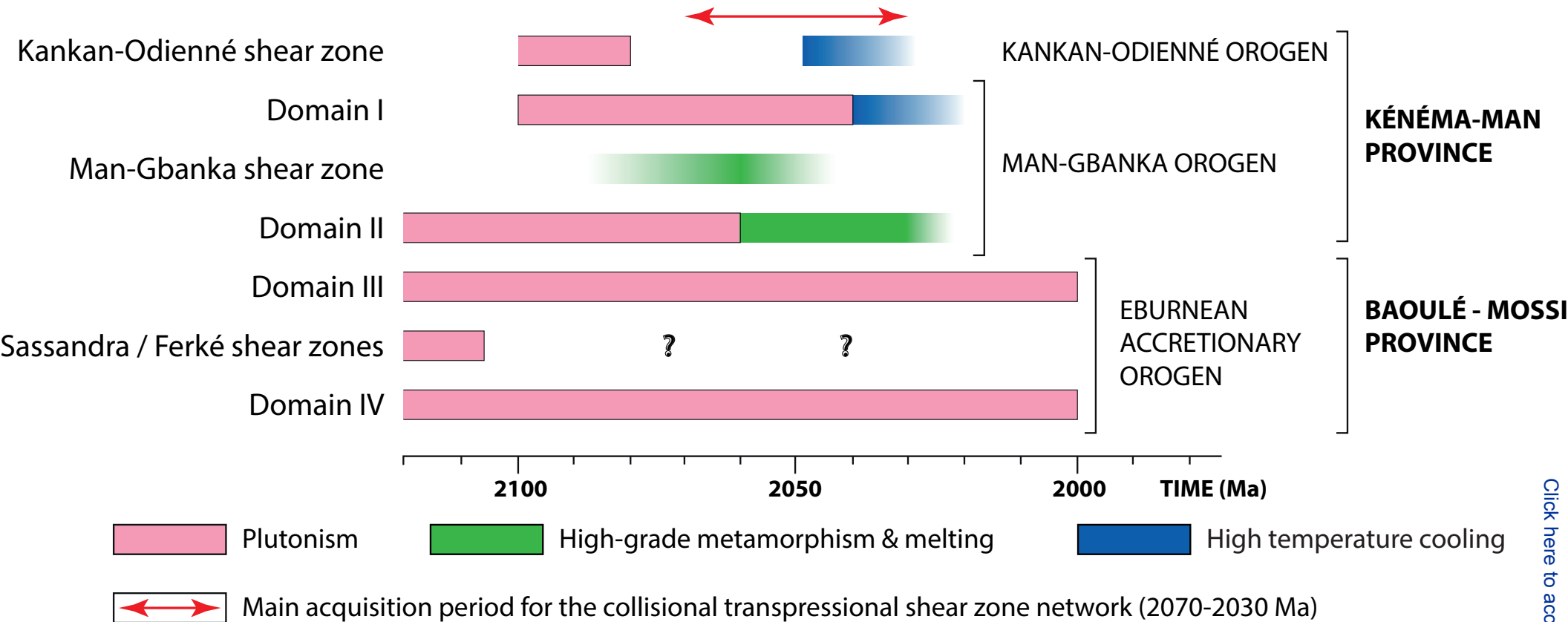


20 km

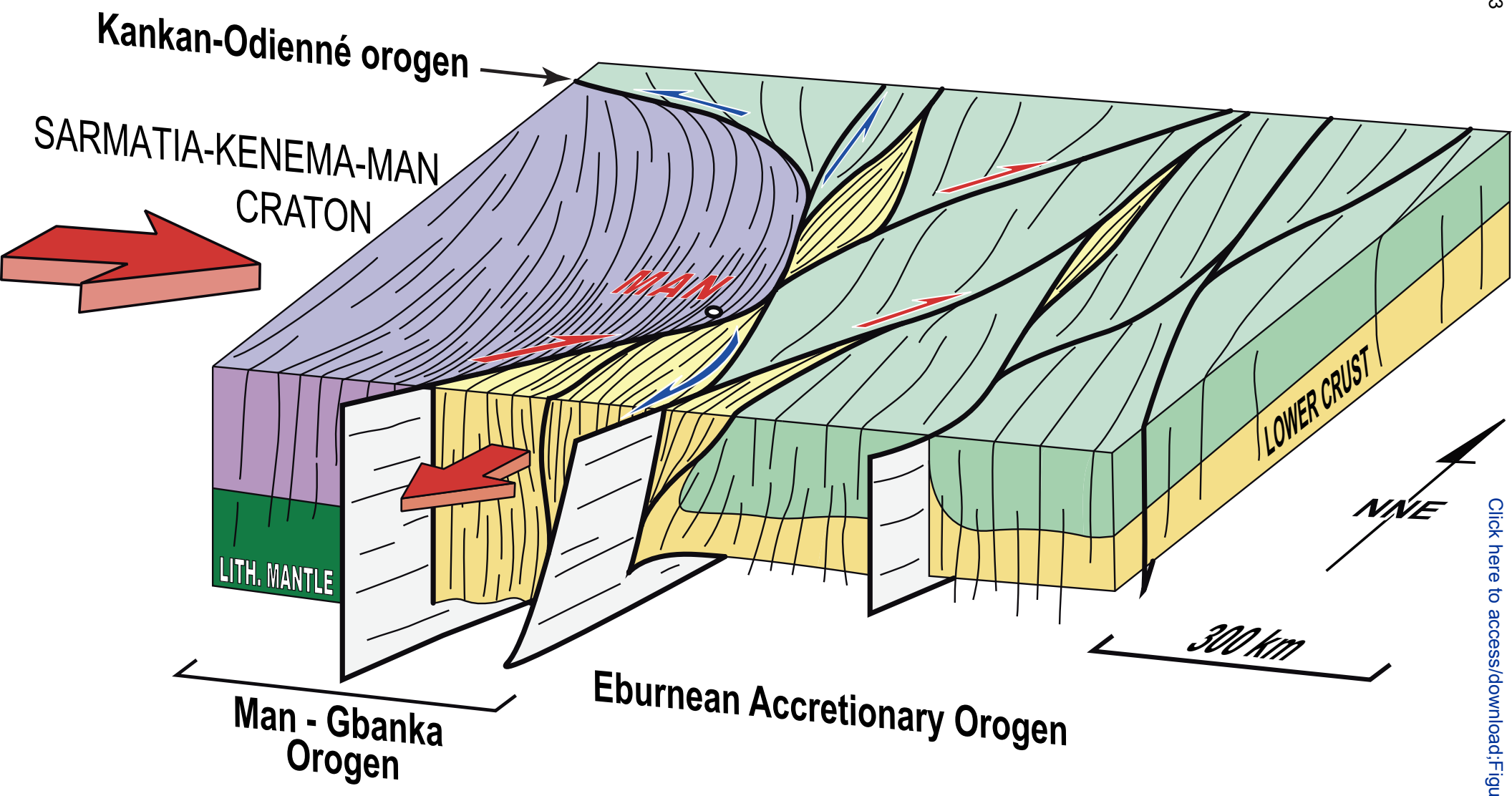




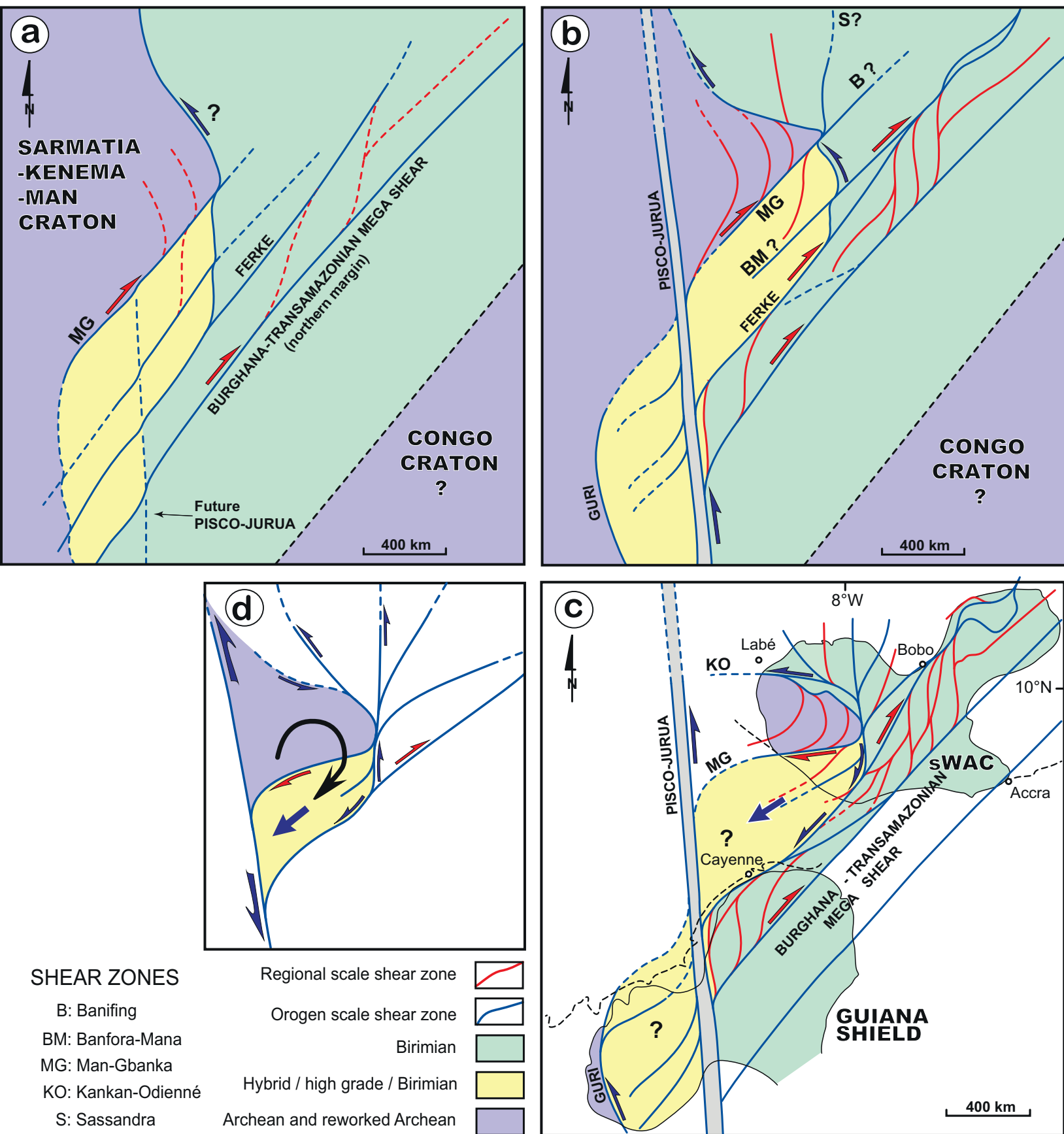
Traoré et al., Fig. 11



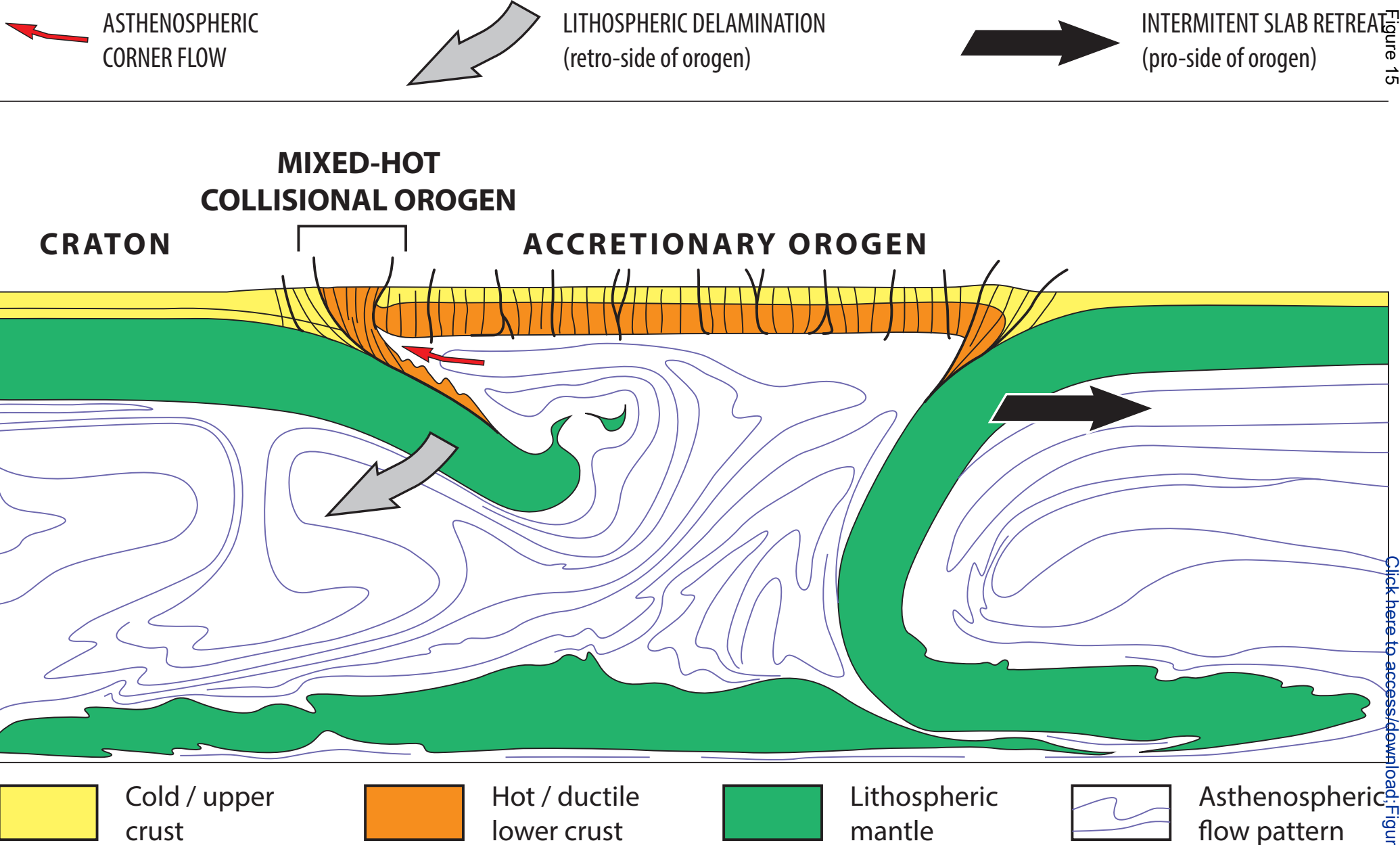
Traoré et al., Fig. 12



Traoré et al., Fig. 13



Traoré et al., Fig. 14



Traoré et al., Fig. 15